



Boosted carbon resistance of ceria-hexaaluminate by in-situ formed $\text{CeFe}_x\text{Al}_{1-x}\text{O}_3$ as oxygen pool for chemical looping dry reforming of methane

Qian Yang^{a,1}, Lihua Chen^{a,1}, Nannan Jin^{a,c}, Yanyan Zhu^{a,*}, Jiahui He^{a,b}, Peijie Zhao^a, Chuande Huang^{b,*}, Liping Wei^a, Xiaoxun Ma^a, Xiaodong Wang^{b,*}

^a School of Chemical Engineering, Northwest University, International Scientific and Technological Cooperation Base of MOST for Clean Utilization of Hydrocarbon Resources, Chemical Engineering Research Center for the Ministry of Education for Advance Use Technology of Shanbei Energy, Xi'an 10069, PR China

^b Key Laboratory of Science and Technology on Applied Catalysis, Dalian Institute of Chemical Physics, Chinese Academy of Sciences, Dalian 116023, PR China

^c China National Offshore Oil Corporation Refining & Zhongjie Petrochemical Company Limited, Hebei 061101, PR China

ARTICLE INFO

Keywords:

Chemical looping dry reforming of methane
Hexaaluminate
Ceria
Carbon resistance
Syngas

ABSTRACT

High potential to carbon deposition over metallic Fe^0 greatly limits the improvement of methane-to-syngas selectivity via chemical looping technology. Herein, we found that the in-situ formed $\text{CeFe}_x\text{Al}_{1-x}\text{O}_3$ over ceria-hexaaluminate as “oxygen pool” could greatly improve carbon resistance even with presence of Fe^0 . Formation of $\text{CeFe}_x\text{Al}_{1-x}\text{O}_3$ only proceeds in ceria-hexaaluminate composite while not occurs in $\text{CeO}_2\text{-Fe}_2\text{O}_3\text{-Al}_2\text{O}_3$, which was probably originated from the strong interaction between CeO_2 and the adjacent Fe and Al ions in $\text{BaFe}_3\text{Al}_9\text{O}_{19}$ hexaaluminate structure. $\text{CeFe}_x\text{Al}_{1-x}\text{O}_3$ with outstanding oxygen ion conduction capacity was in close contact with metallic Fe^0 exsolved from Fe-hexaaluminate in a unique $\text{CeFe}_x\text{Al}_{1-x}\text{O}_3/\text{Fe}^0/\text{hexaaluminate}$ sandwich-like structure, which provided a convenient pathway for $\text{CeFe}_x\text{Al}_{1-x}\text{O}_3$ as “oxygen pool” to supply sufficient oxygen for in-time oxidation of carbon over adjacent Fe^0 . Consequently, the recycled ceria-hexaaluminate displayed both outstanding carbon resistance and high CH_4 conversion (~90%) with enhanced syngas yield that 105% and 72% higher than $\text{CeO}_2\text{-Fe}_2\text{O}_3\text{-Al}_2\text{O}_3$ oxide and Fe-hexaaluminate, respectively.

1. Introduction

Conversion of both CH_4 and CO_2 has been greatly motivated by the commitment of becoming “carbon neutral” and the increasing capacity of shale gas in recent years. Chemical-looping dry reforming (CLDR) of methane is a promising technology, since it not only converts CH_4 into F-T ready syngas with ideal H_2/CO ratio (~2) but also converts greenhouse gas CO_2 into CO based on the circulation of oxygen carrier (OC, typically a transition metal oxide) [1–4]. Different from the co-feeding mode of traditional dry reforming of methane (H_2/CO ~1) [5,6], the avoidance of direct contact between CH_4 and CO_2 in CLDR enables an increase in syngas selectivity via suppressing reverse water gas shift reaction [7]. Besides, it is capable of handling the dilute CO_2 stream [8, 9], which makes it rather unique among current CO_2 utilization technologies. The inexpensive and environmentally-friendly Fe-based oxide holds the virtue of the highest CO_2 conversion capacity over a broad

operating temperature window (700–1800 °C) [8], Fe-based OC was considered as one of the promising candidates for CLDR process.

In CLDR without gas-phase oxygen molecules, OC is not only utilized to active CH_4 but also supply oxygen for methane anaerobic oxidation to produce syngas [10–13]. Unfortunately, Fe-based oxide usually exhibits low CH_4 reactivity, probably caused by the repeated atomic rearrangement [14]. To improve the CH_4 reactivity, various noble metals (such as, Pt, Rh) and non-noble metals (such as, La, Cu, Ni) were added into the iron oxide to create active sites for CH_4 activation [1,15–19]. Although metallic Fe^0 itself is highly reactive towards C-H bond activation [20, 21], the reduction degree of Fe-based OCs needs to be carefully controlled to avoid deep reduction of iron cations to metallic Fe^0 . This is because the appearance of metallic Fe^0 could greatly enhance the C-H bond activation ability, but the mobility of lattice oxygen from bulk to surface generally became slower as increasing the reduction degree [22]. Such a mismatch between the high C-H bond activation ability of

* Corresponding authors.

E-mail addresses: zhuyanyan@nwnu.edu.cn (Y. Zhu), huangchuande@dicp.ac.cn (C. Huang), xdwang@dicp.ac.cn (X. Wang).

¹ Both authors contributed to this work equally.

Fe^0 and the insufficient oxygen supply under deep reduction condition easily results in the carbon formation caused by methane cracking ($\text{CH}_4 = 2 \text{H}_2 + \text{C}$). Once the rate of carbon formation is faster than that of carbon elimination ($\text{C} + \text{O}_{\text{Lattice}} = \text{CO}$) via oxidizing carbon by lattice oxygen into gaseous CO, carbon will continuously accumulate and cover the active sites for CH_4 reaction, leading to the decrease of lattice oxygen supply and degradation of OCs. Therefore, high potential to carbon deposition over metallic Fe^0 greatly limits the improvement of methane-to-syngas selectivity via chemical looping technology.

So far, most of the reports have been concentrated on the ceria-based and perovskite-based OCs due to their good oxygen ion conductivity [1, 3,7,12,13,20,23–26], which is beneficial for the in-time carbon oxidation and elimination. Li et al. [27] found that the chemical reaction between surface exposed Fe_2O_3 and $\text{Fe}_x\text{Ce}_{1-x}\text{O}_2$ (Fe ions entered into CeO_2 lattice) greatly enhanced the methane-to-syngas conversion, and deposited carbon could be oxidized in time to CO by the activated oxygen of Ce-Fe oxides. Tang et al. [28] reported that the incorporation of rare earth (i.e., La and Ce) into $\text{Fe}_2\text{O}_3/\text{Al}_2\text{O}_3$ induced the generation of LaFeO_3 and CeFeO_3 perovskites with abundant oxygen defects, which facilitated the lattice oxygen transfer kinetics and carbon resistance. Besides, in situ encapsulation of metallic Fe^0 in Fe-based perovskite could notably restrain the carbon formation via minimizing the direct contact between CH_4 and surface Fe^0 at the expense of relatively low CH_4 conversion due to the absence of surface Fe^0 [29,30]. Although much progress has been made, ceria-based and perovskite-based OCs usually suffer from severe sintering of particles and the decrease of surface area due to phase segregation during the successive redox reactions. For example, the surface areas of $\text{CeO}_2\text{-Fe}_2\text{O}_3$ and LaFeO_3 OCs sharply decreased from $14.7 \text{ m}^2\cdot\text{g}^{-1}$ and $3.8\text{--}30 \text{ m}^2\cdot\text{g}^{-1}$ in the fresh samples to $0.4 \text{ m}^2\cdot\text{g}^{-1}$ and $0.2\text{--}1.0 \text{ m}^2\cdot\text{g}^{-1}$ after 10 CH_4 /air redox cycles, respectively [27,31]. The sintering and low surface area greatly limit the lattice oxygen mobility and thus decrease the longevity [32]. Therefore, it is still challenging to improve the CH_4 activation, carbon resistance (especially for the deeply reduced OC with presence of Fe^0) and redox stability, simultaneously.

Hexaaluminates with high thermal stability are generally used for high-temperature catalysts [33–35] and the use of Fe-substituted hexaaluminate in chemical looping as OC is a relatively new topic. In our recent works [36,37], Fe-substituted hexaaluminates with layer structure were verified to exhibit excellent structure stability even during the CH_4 reduction process with syngas generation via the charge compensation mechanism, and the surface area of hexaaluminate still remained $9\text{--}20 \text{ m}^2\cdot\text{g}^{-1}$ even after 10–50 CH_4/CO_2 redox cycles. Ceria has the ability to release/acquire oxygen through redox process involving the $\text{Ce}^{4+}/\text{Ce}^{3+}$ couple [23,38]. Combining CeO_2 with hexaaluminate may create a promising oxygen storage material for CLDR technology. In present work, ceria modified $\text{BaFe}_3\text{Al}_9\text{O}_{19}$ hexaaluminate ($\text{CeO}_2\text{-BF3}$) was designed as OC for CLDR with pure CeO_2 , $\text{BaFe}_3\text{Al}_9\text{O}_{19}$ hexaaluminate (BF3), and $\text{CeO}_2\text{-Fe}_2\text{O}_3\text{-Al}_2\text{O}_3$ (Ce-Fe-Al) oxide for comparison. It is surprising to find that the formation of $\text{CeFe}_x\text{Al}_{1-x}\text{O}_3$ only proceeds in $\text{CeO}_2\text{-BF3}$ while not occurs in Ce-Fe-Al. Moreover, a unique $\text{CeFe}_x\text{Al}_{1-x}\text{O}_3/\text{Fe}^0$ /hexaaluminate sandwich-like structure formed during the successive CH_4/CO_2 redox process of $\text{CeO}_2\text{-BF3}$ OC, where metallic Fe^0 exsolved from Fe-hexaaluminate acted as active site for methane activation, and $\text{CeFe}_x\text{Al}_{1-x}\text{O}_3$ with outstanding oxygen ion conduction capacity acted as “oxygen pool” to supply sufficient oxygen for in-time oxidation of carbon over adjacent Fe^0 . As a result, the recycled $\text{CeO}_2\text{-BF3}$ OC presented both outstanding carbon resistance and high methane conversion ($\sim 90\%$) for syngas production during the successive redox cycles, which was 105% and 72% higher than Ce-Fe-Al oxide and hexaaluminate, respectively. On the basis of various characterization (e.g., XRD, Rietveld refinement, HRTEM, XPS and DFT calculation), the structure-activity relationship and reaction mechanism were provided.

2. Experimental

2.1. Oxygen carriers (OCs) preparation

$\text{BaFe}_3\text{Al}_9\text{O}_{19}$ (denoted as BF3) hexaaluminate was prepared by the chemical co-precipitation method. The starting materials of $\text{Ba}(\text{NO}_3)_2$, $\text{Fe}(\text{NO}_3)_3\cdot 9 \text{H}_2\text{O}$ and $\text{Al}(\text{NO}_3)_3\cdot 9 \text{H}_2\text{O}$ (Aldrich, purity >98%) with a molar ratio of 1: 3: 9 were dissolved individually in deionized water at 60°C . Subsequently, the mixture was added into a saturated aqueous solution of $(\text{NH}_4)_2\text{CO}_3$ under strong stirring to form the hexaaluminate precursor precipitate. After continuous stirring at 60°C for 6 h, the slurry was aged at room temperature for 1 h. Then the precipitate was filtered, washed and dried at 120°C for 12 h. Finally, the sample was calcined at high-temperature of 1100°C for 4 h under ambient air to obtain the BF3 hexaaluminate.

The ceria modified $\text{BaFe}_3\text{Al}_9\text{O}_{19}$ hexaaluminate (denoted as $\text{CeO}_2\text{-BF3}$) sample was prepared by the method of impregnation precipitation. A desired amount of $\text{Ce}(\text{NO}_3)_3\cdot 6 \text{H}_2\text{O}$ (the molar ratio of Ce/Fe is 3:7) was dissolved in the deionized water. Then, the BF3 hexaaluminate was added to the $\text{Ce}(\text{NO}_3)_3$ solution and stirred for 2 h at room temperature. Subsequently, excess $(\text{NH}_4)_2\text{CO}_3$ is added to the solution to form suspension at 60°C . The precipitate was filtered, washed, and dried at 120°C overnight. This object was finally calcined at 900°C for 4 h under air atmosphere to obtain the $\text{CeO}_2\text{-BF3}$ OC.

For comparison, both $\text{CeO}_2\text{-Fe}_2\text{O}_3\text{-Al}_2\text{O}_3$ (denoted as Ce-Fe-Al) and CeO_2 were prepared by the chemical co-precipitation method. Typically, to prepare $\text{CeO}_2\text{-Fe}_2\text{O}_3\text{-Al}_2\text{O}_3$, $\text{Ce}(\text{NO}_3)_3\cdot 6 \text{H}_2\text{O}$, $\text{Fe}(\text{NO}_3)_3\cdot 9 \text{H}_2\text{O}$ and $\text{Al}(\text{NO}_3)_3\cdot 9 \text{H}_2\text{O}$ with a molar ratio of 3:7:21 (same ratio to $\text{CeO}_2\text{-BF3}$, without Ba) were individually dissolved in deionized water at 60°C , and then precipitated with saturated $(\text{NH}_4)_2\text{CO}_3$ as a precipitating agent. Upon stirring, aging, filtering, washing, and drying at 120°C , the obtained precipitate material was finally calcined at 900°C for 4 h in a muffle furnace under air atmosphere. CeO_2 was also prepared by similar procedure but without addition of $\text{Fe}(\text{NO}_3)_3\cdot 9 \text{H}_2\text{O}$ and $\text{Al}(\text{NO}_3)_3\cdot 9 \text{H}_2\text{O}$ in the starting materials.

2.2. Oxygen carrier characterization

The X-ray diffraction (XRD) patterns of OCs were recorded by a PANalytical X'pert-Pro Super powder X-ray diffractometer ($U = 40 \text{ kV}$, $I = 40 \text{ mA}$) using $\text{Cu-K}\alpha$ radiation ($\lambda = 0.15432 \text{ nm}$). The diffraction angle was scanned in the region of $10^\circ \sim 80^\circ$. In order to alleviate the possible preferential orientation arising from the anisotropic planar crystallites of hexaaluminates, the hexaaluminate-based sample was grinded roundly to a fine powder and then pressed lightly using a glass slide before the XRD test. Crystalline size was estimated by the Scherrer equation. Phase composition was identified by Rietveld full-profile analysis using Highscore Plus software.

Both hydrogen temperature-programmed reduction ($\text{H}_2\text{-TPR}$) and methane temperature-programmed reduction ($\text{CH}_4\text{-TPR}$) were conducted on a fixed-bed reactor. 300 mg OC was exposed to a flow of 5% H_2/Ar ($15 \text{ mL}\cdot\text{min}^{-1}$) or a flow of 5% CH_4/Ar ($15 \text{ mL}\cdot\text{min}^{-1}$) from 200 or 300–900 $^\circ\text{C}$ with a heating rate of $10^\circ\text{C}\cdot\text{min}^{-1}$. The outlet gases from both $\text{H}_2\text{-TPR}$ and $\text{CH}_4\text{-TPR}$ were analyzed by an online mass spectrometer (IPI GAM 200).

Scanning transmission electron microscopy (STEM), high-angle annular dark-field scanning transmission electron microscopy (HAADF-STEM), line-scan and elemental mapping were performed using a field-emission transmission electron microscope (JEOL JEM-2100 F). The samples were dispersed in ethanol and then dropped onto a carbon-coated 300 mesh copper grid.

$\text{CH}_4\text{-IR}$ profiles were obtained on C600 NDIR infrared gas analyzer. The OC was firstly treated in a fixed-bed reactor at 300°C for 1 h under N_2 atmosphere and then the temperature increased from 300 to 900°C at a heating rate of $10^\circ\text{C}\cdot\text{min}^{-1}$. The concentration signals of produced CO and CO_2 were detected and recorded in real time by the system

software.

X-ray photoelectron spectroscopy (XPS) analysis was detected on a Kratos AXIS UL TRA spectrometer equipped with a monochromatic Al K α source. The external carbon pollution (C1s, 284.8 eV) was used as XPS signal calibration. The samples after 20 CH₄/CO₂ cycles were cooled to room temperature in an inert atmosphere for measurement.

2.3. Reactivity and recyclability evaluation

The isothermal reaction as a function of time between methane and different OCs was carried out in a fixed-bed reactor, which was assembled in an electric heating furnace at atmospheric pressure. Oxygen carriers (300 mg, 20–40 mesh) were placed into a quartz tube with 6 mm inside diameter and heated from room temperature to 900 °C at a rate of 10 °C·min⁻¹ in Ar atmosphere. After the temperature was stable at 900 °C, methane (5 vol% CH₄, 15 mL·min⁻¹, Ar as balance gas) was introduced to the reaction tube for 7 min.

The recyclability evaluations of OCs were performed by exposing the OCs to alternating CH₄ and CO₂ atmosphere in a fixed-bed reactor at 900 °C. Firstly, 5% CH₄/Ar (15 mL·min⁻¹) was introduced to reduce OCs for 7 min. After argon purging for 5 min, the 5% CO₂/Ar (20 mL·min⁻¹) was used to regenerate the OCs. The gas stream was switched periodically between Ar and the gas containing CH₄ (reduction step) or CO₂ (oxidation step) for 20 times. In certain case, O₂ (5% O₂/Ar, 20 mL·min⁻¹) instead of CO₂ was introduced to restore the reduced OC for comparison. Sometimes, an additional O₂-oxidation step was performed after CH₄/CO₂ redox cycle with the aim to investigate the condition of carbon removal by CO₂ over the CO₂-regenerated OC. The concentrations of outlet gases (CH₄, CO₂, CO, H₂) were detected online by a mass spectrometer (IPI GAM 200). The mass spectrometer signals were calibrated accurately before the experiment using a calibration gas with known composition.

The conversion, selectivity of various gaseous products, the molar ratio of H₂/CO, the amount of converted oxygen (O_t, mmol·g⁻¹) and the syngas yield (Y_s, mmol·g⁻¹) were calculated based on the equations described in our previous reports [37,39]. The amount of accumulated carbon was calculated from the molar ratio of H₂/CO exceeding 2.

2.4. Computational details

Density functional theory (DFT) calculations were carried out using dmol³ module of Materials Studio [40]. The generalized gradient approximation (GGA) with the Perdew–Burke–Ernzerhof (PBE) functional was applied to evaluate the electron exchange and correlation [41]. For the geometry optimization, the convergences of the energy, maximum force, and maximum displacement were set as 2×10^{-6} Ha, 2×10^{-3} Ha/Å, and 5×10^{-3} Å, respectively.

To determine the effect of Fe doping on the oxygen mobility, the models of both CeAlO₃ and CeFe_{0.25}Al_{0.75}O₃ with cubic structure were built, and the k-grid sampling of the Brillouin zone was set to $4 \times 4 \times 4$ for the bulk. Based on geometric optimization, the total energy of different doping sites of Fe in CeAlO₃ was calculated, and the most stable doping structure was determined. The supercell ($2 \times 2 \times 2$) of the simple perovskite unit cell containing 40 atoms was used and the free energy of oxygen vacancy formation ($E_{f,vac}$) was defined as:

$$E_{f,vac} = E_{defective} + 1/2\mu_{O_2} - E_{perfect}$$

where $E_{defective}$, μ_{O_2} , and $E_{perfect}$ are the total energy of the system containing oxygen vacancy, the chemical potential of O₂, and the total energy of the perfect system, respectively.

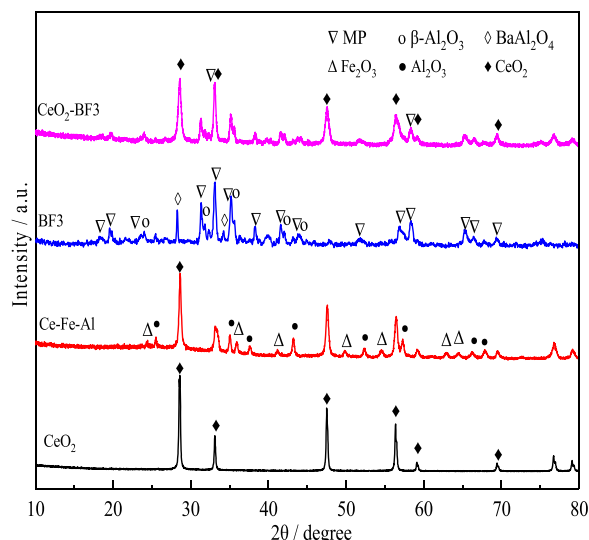


Fig. 1. X-ray diffraction patterns of fresh CeO₂, Ce-Fe-Al, BF₃ and CeO₂-BF₃ OCs.

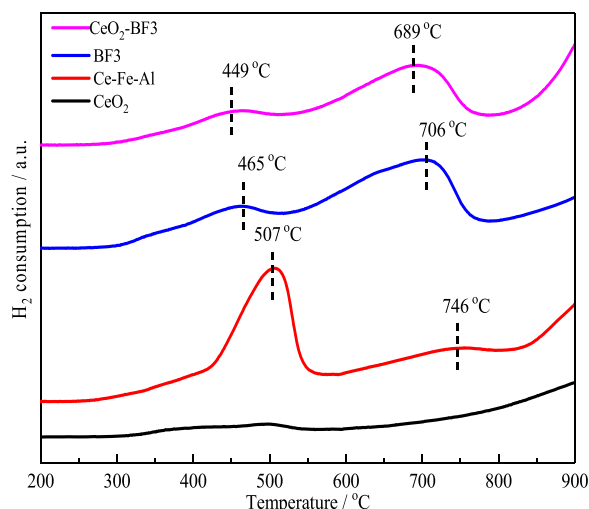


Fig. 2. H₂-TPR profiles of fresh CeO₂, Ce-Fe-Al, BF₃, and CeO₂-BF₃ OCs.

3. Results

3.1. Effect of CeO₂ introduction on structure and oxygen mobility

3.1.1. XRD

Fig. 1 shows the diffraction patterns of fresh CeO₂, Ce-Fe-Al, BF₃ and composite CeO₂-BF₃ OCs. CeO₂ displayed the typical features of a face-centered cubic fluorite-structure. For Ce-Fe-Al OC, besides CeO₂, characteristic peaks of α -Fe₂O₃ and α -Al₂O₃ were also observed. BF₃ presented the co-existence of both β -Al₂O₃ and magnetoplumbite (MP) type hexaaluminate. No iron oxide was identified in BF₃, indicating high dispersion of Fe species. The expansion of lattice constant of hexaaluminate suggested that Fe ions with larger ion radius (0.64 Å) were incorporated into the hexaaluminate lattice by replacing the smaller Al ions (0.51 Å), in agreement with our previous works [42,43]. The composite CeO₂-BF₃ OC exhibited multiphase CeO₂, Fe-substituted MP and β -Al₂O₃ hexaaluminates. The crystalline size of CeO₂ over CeO₂-BF₃ was about 17 nm, which was much smaller than that in both pure CeO₂ (47 nm) and Ce-Fe-Al (25 nm) OCs. This suggested an intimate interaction between CeO₂ and BF₃, which facilitated better dispersion for CeO₂ and may modulate the redox performance of this composite OC.

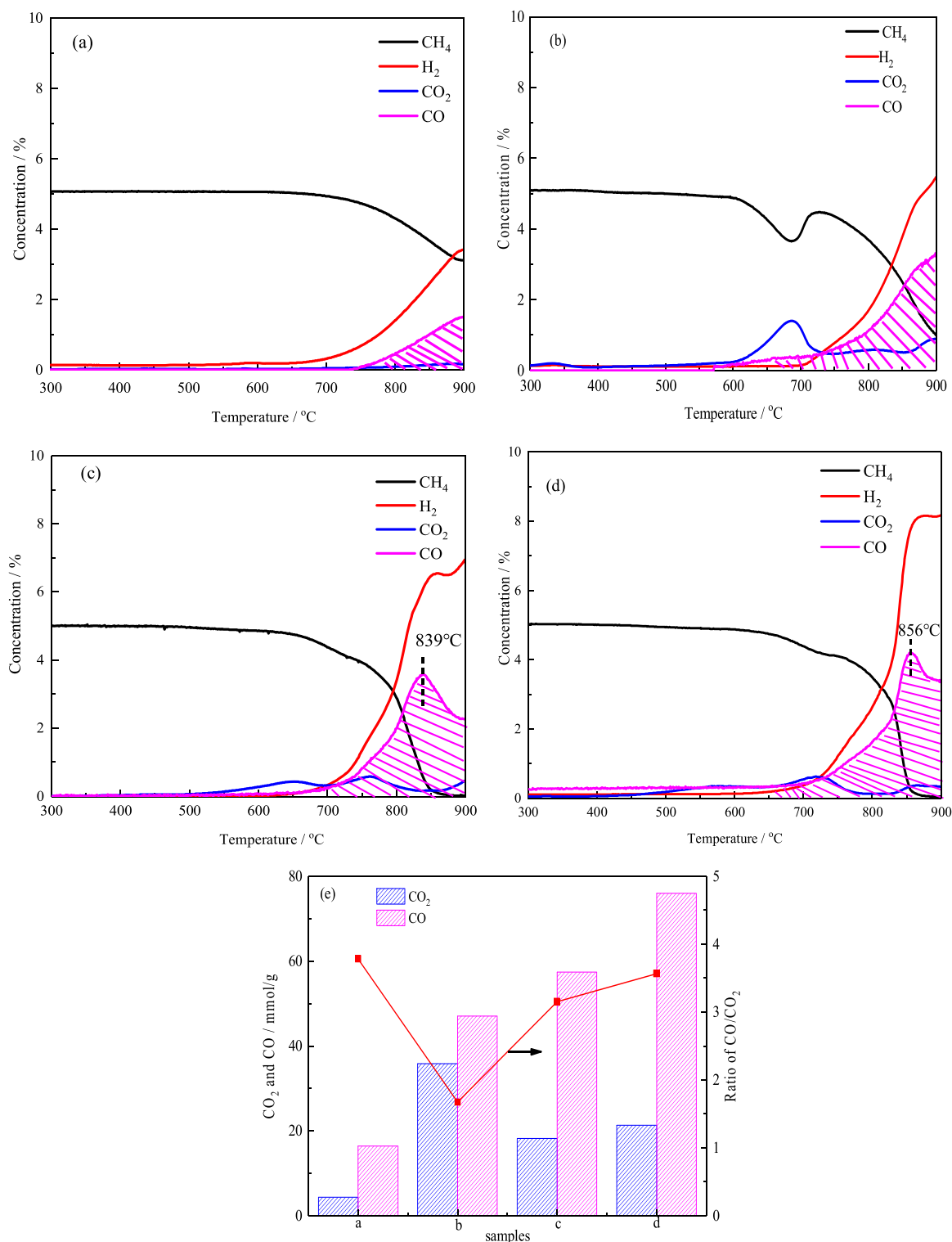


Fig. 3. CH₄-TPR profiles of fresh (a) CeO₂, (b) Ce-Fe-Al, (c) BF₃, (d) CeO₂-BF₃ OCs, and (e) the produced CO and CO₂ and the ratio of CO/CO₂ over all OCs.

3.1.2. H₂-TPR

Oxygen mobility of OCs is very important for methane anaerobic oxidation in CLDR, which was investigated by H₂-TPR. As shown in Fig. 2, single CeO₂ showed low reducibility. Ce-Fe-Al presented the overlapping reduction of Fe (Fe₂O₃→Fe₃O₄, Fe₃O₄→FeO, FeO→Fe⁰) and Ce species [44], and H₂ consumption peak around 507 °C was mainly attributed to the reduction of large α-Fe₂O₃ particles (~33 nm estimated from Fig. 1). H₂-TPR patterns of both BF₃ and CeO₂-BF₃ are similar,

indicating the main contribution of Fe-substituted hexaaluminate to the reducibility [45,46]. Compared to Ce-Fe-Al OC, both BF₃ and CeO₂-BF₃ exhibited much lower reduction temperature (449–465 °C), which should be related to the high dispersion of Fe species in hexaaluminate. In particular, reduction peaks of CeO₂-BF₃ begun at lower temperature than pure BF₃, suggesting that the chemical interaction between CeO₂ and BF₃ enhanced the oxygen mobility.

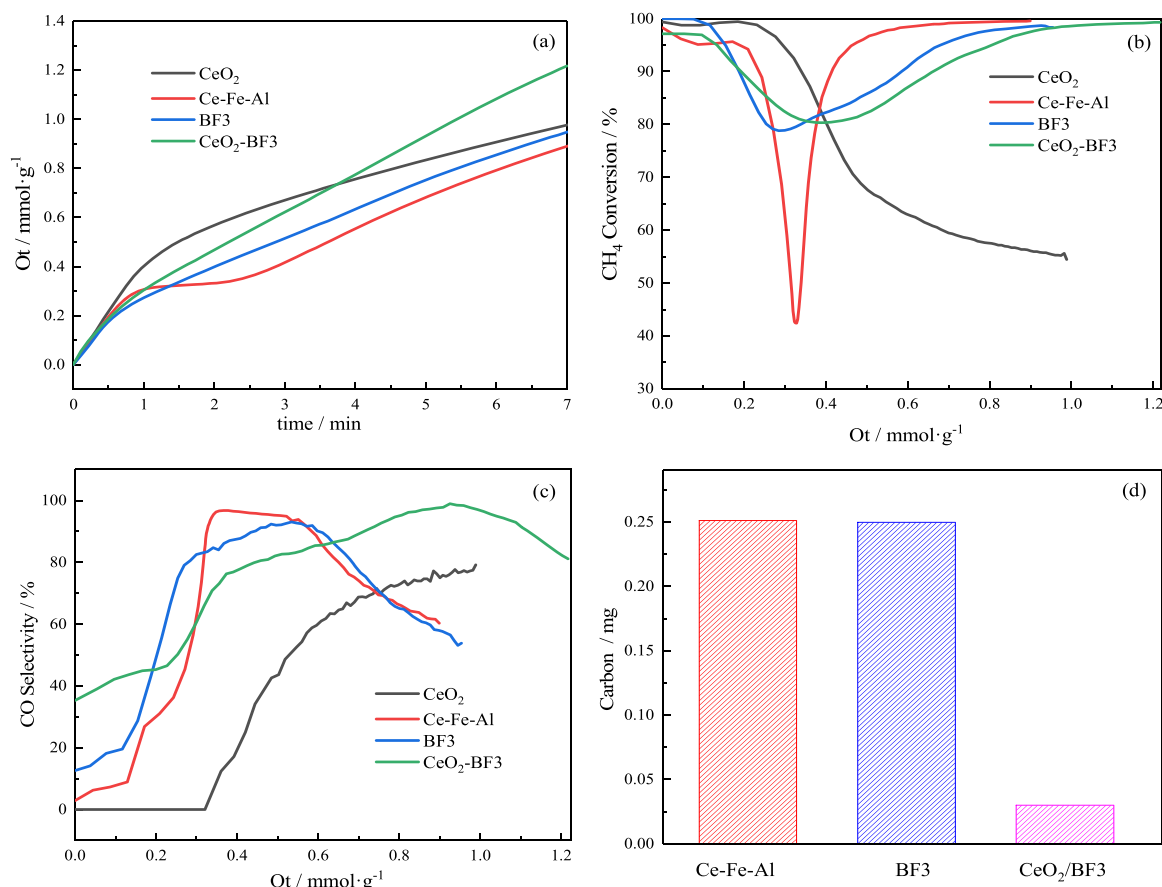


Fig. 4. Performance of methane anaerobic oxidation of CeO₂, Ce-Fe-Al, BF₃, and CeO₂-BF₃ OCs during 5th CH₄ reduction at 900 °C: (a) kinetic curves of O_t with time, (b) CH₄ conversion, and (c) CO selectivity as a function of O_t, (d) the content of accumulated carbon within 7 min.

3.2. Redox reaction behavior of OCs

3.2.1. CH₄-TPR

The reactivity for methane anaerobic oxidation to produce syngas was firstly investigated by CH₄-TPR (Fig. 3). Unreacted CH₄ concentration over CeO₂ and Ce-Fe-Al OCs was still high from 750 to 900 °C, but that of hexaaluminate-containing BF₃ and CeO₂-BF₃ sharply decreased from 750 °C and almost disappeared during 800–900 °C, indicating the higher CH₄ activity. Different from the large CO₂ peak of Ce-Fe-Al OC at 600–750 °C due to the reduction of Fe₂O₃→Fe₃O₄ with typical features giving deep oxidation product [47], the CO₂ signals (Fig. 3c and d) were obviously weakened when Fe cations are confined in BF₃ hexaaluminate matrix. Compared to BF₃, CeO₂-BF₃ exhibited the higher CO/CO₂ ratio of 3.57 (Fig. 3e), indicating the higher CO selectivity of CeO₂-BF₃ OC, since CO/CO₂ ratio represents the CO selectivity to some degree. It is noted that the formation of H₂ was ahead of CO over four OCs, suggesting that CH₄ decomposition (CH₄→C+2 H₂) occurred firstly, which was followed by CO formation via the oxidation of carbon by the lattice oxygen of OCs. The decrease of CO concentration as rising temperature indicated the carbon deposition due to insufficient lattice oxygen supply. Compared to 839 °C of CO peak over BF₃, CO concentration over CeO₂-BF₃ peaked up to 856 °C, indicating the better carbon-resistance of CeO₂-BF₃.

3.2.2. Isothermal kinetic behavior

Fig. S1 shows the isothermal kinetic curves of CeO₂, Ce-Fe-Al, BF₃, and CeO₂-BF₃ OCs with time during 5th CH₄ reduction at 900 °C in a fixed-bed reactor. One can see that the total oxidation, partial oxidation, and pyrolysis of CH₄ occurred in sequence as the OCs were progressively reduced, since the OC acts as an oxygen donor for methane oxidation in

the chemical looping process without gaseous oxidants. The amount of converted oxygen (O_t, mmol·g⁻¹) for methane total and partial oxidation was calculated, which represents the reduction degree to some degree. Fig. 4a shows the kinetic curves of O_t during the CH₄ reduction process. Compared to CeO₂, Ce-Fe-Al and BF₃ OCs (0.90–0.99 mmol·g⁻¹), the CeO₂-BF₃ exhibited higher O_t (1.22 mmol·g⁻¹), indicating that more lattice oxygen was exacted from CeO₂-BF₃ OC under the same reduction time (7 min). Fig. 4b-d shows the CH₄ conversion and CO selectivity of four OCs as a function of O_t as well as the accumulated carbon within 7 min. The CH₄ conversion of CeO₂ gradually decreased (100 →55%) as rising O_t, indicating the insufficient oxygen supply at the deeper reduction degree. For Ce-Fe-Al OC, there is a sharp decline and increase of CH₄ conversion from 0.2 to 0.6 mmol·g⁻¹ with the increase of corresponding CO selectivity, indicating the partial oxidation of methane. The sharp decline of CH₄ conversion of Ce-Fe-Al OC was attributed to the rapid consumption of absorption oxygen or surface Fe₂O₃, while the bulk lattice oxygen can not timely release to supply this consumption. For BF₃ and CeO₂-BF₃ OCs, the decrease of CH₄ conversion was greatly alleviated. Afterwards, although both Ce-Fe-Al and BF₃ OCs kept high CH₄ conversion, the CO selectivity sharply decreased from 0.6 mmol·g⁻¹ O_t, indicating the CH₄ pyrolysis became favored under the deeper reduction degree. However, the CO selectivity continuously increased over CeO₂-BF₃ OC even under the deep reduction of 0.6–0.9 mmol·g⁻¹ O_t, indicating the higher resistance of carbon deposition of CeO₂-BF₃, which was further supported by Fig. 4d. Compared to the high content of accumulated carbon (0.25 mg) over Ce-Fe-Al and BF₃ OCs, the accumulated carbon of CeO₂-BF₃ within 7 min was only 0.03 mg. In a word, CeO₂-BF₃ could exact more lattice oxygen under the same reduction time (7 min), and exhibited higher CO selectivity and carbon-resistance with high CH₄

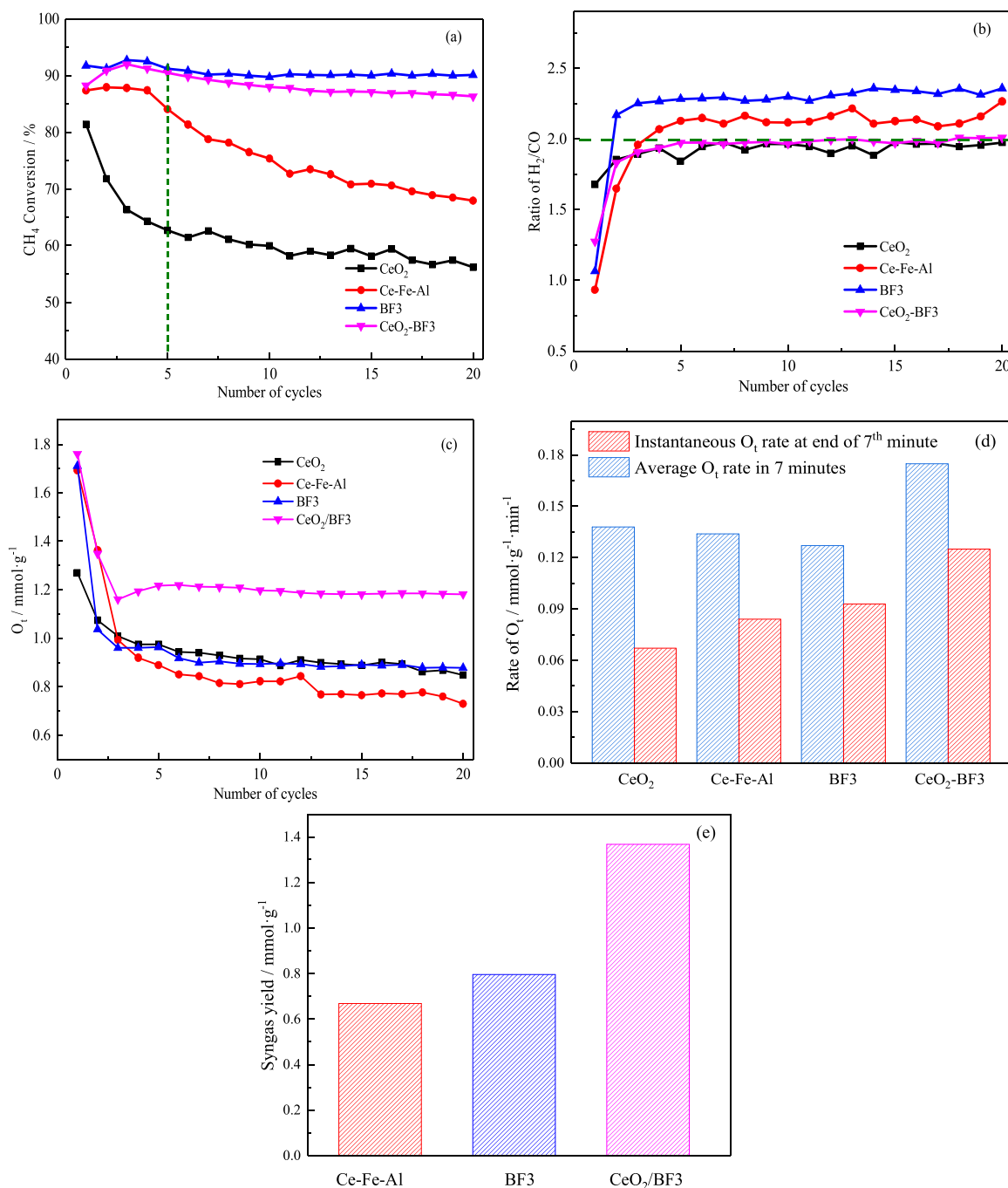


Fig. 5. (a) CH₄ conversion, (b) ratio of H₂/CO, (c) amount of converted oxygen (O_I) as a function of cycle number over CeO₂, Ce-Fe-Al, BF₃ and CeO₂-BF₃ OCs during the successive CH₄/CO₂ redox cycles at 900 °C; (d) average O_I rate within 7 min and instantaneous O_I rate at end of 7th minute and (e) the syngas yield before carbon deposition during the 5th methane-to-syngas conversion.

activity even under the deeper reduction degree.

3.2.3. Successive redox reactions in fixed-bed reactors

Fig. 5 displays the successive performance of four OCs for methane anaerobic oxidation to produce syngas. CH₄ conversion over fresh CeO₂ (81%) rapidly decreased to 63% during the first five redox cycles. The rapid decrease of CH₄ conversion was inhibited over Ce-Fe-Al to some extent, but carbon deposition with H₂/CO ratio above 2 was observed (Fig. 5b). In comparison, hexaaluminate-containing both BF₃ and CeO₂-BF₃ OCs still presented high CH₄ conversion (~90%) even after 20 cyclic operations. Unfortunately, the H₂/CO ratio of BF₃ hexaaluminate was much higher (2.16–2.36, Fig. 5b) than the ideal value (2), revealing

that CH₄ cracking occurred and the formed carbon failed to be oxidized in time by lattice oxygen. Compared to the high H₂/CO ratio of BF₃, the H₂/CO ratio over CeO₂-BF₃ OC is close to the ideal value (2), indicating the carbon deposition was greatly suppressed. Moreover, the content of converted oxygen (O_I) of CeO₂-BF₃ is higher than BF₃ (1.18–1.34 mmol.g⁻¹ for CeO₂-BF₃ vs 0.88–1.04 mmol.g⁻¹ for BF₃, Fig. 5c), indicating the higher lattice oxygen supply capacity of CeO₂-BF₃, which may be caused by its high carbon resistance, since the in-time removal of deposited carbon over the active sites is beneficial for the absorption and activation of more methane molecules. Take the 5th reduction for example, the average and instantaneous O_I rates were further compared and the results were displayed in Fig. 5d. Among the

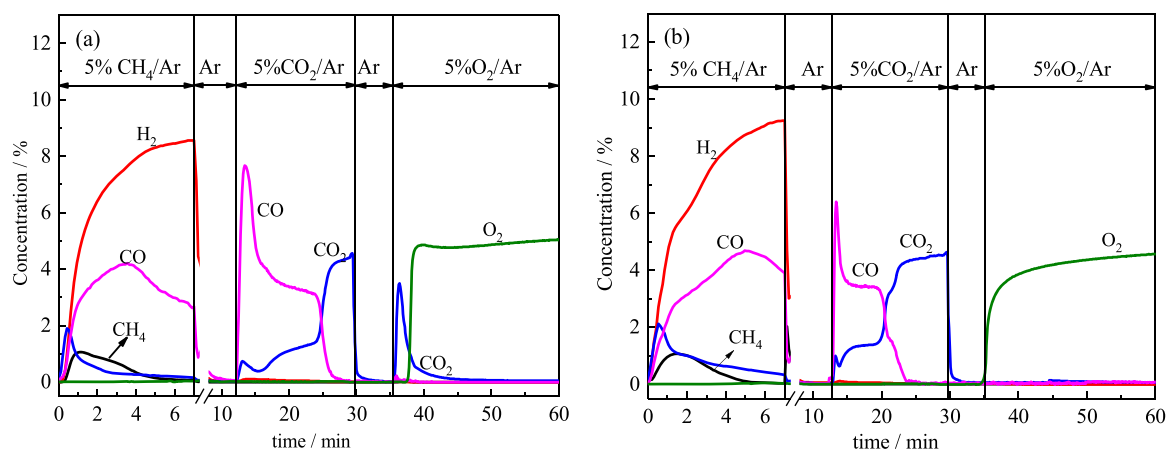


Fig. 6. The product profiles of (a) BF3 and (b) CeO₂-BF3 OCs in the 5th CH₄/CO₂ cycle with additional O₂ oxidation.

four OCs, CeO₂-BF3 OC exhibited the highest average O_i rate (0.175 mmol·g⁻¹·min⁻¹) within 7 min, and the instantaneous O_i rate at the end of 7th minute of CeO₂-BF3 still reached up to 0.125 mmol·g⁻¹·min⁻¹ even under the deeper reduction degree, almost two times higher than CeO₂ (0.067 mmol·g⁻¹·min⁻¹). The methane-to-syngas productivity before carbon deposition (transient H₂/CO ratio above 2) over recycled Ce-Fe-Al, BF3 and CeO₂-BF3 OCs are compared in Fig. 5e. CeO₂-BF3 exhibited the highest syngas yield, which was about 105% and 72% higher than Ce-Fe-Al oxide and pure BF3 hexaaluminate, respectively. In a word, the recycled CeO₂-BF3 is very effective in both improving methane conversion and suppressing carbon deposition. The CeO₂-BF3 OC was carried out 30 successive CH₄/CO₂ redox cycles due to the best performance. As shown in Fig. S2, CeO₂-BF3 OC still presented high methane conversion (above 85%) and ideal ratio of H₂/CO (close to 2) in 30 redox cycles, which further confirmed the excellent redox stability of CeO₂-BF3 OC with high methane conversion and high resistance to carbon deposition.

Subsequently, the reduced OCs were oxidized by CO₂ to restore the exhausted lattice oxygen and remove the possible carbon deposition. As shown in Fig. S3, although the “burn off” of deposited carbon over BF3 devoted to CO₂ conversion (C+CO₂→2CO), CeO₂-BF3 OC still exhibited the highest CO₂ conversion and excellent cyclic stability with close oxidation kinetic curves during the successive CH₄/CO₂ redox cycles. In order to investigate the status of carbon removal by CO₂, we performed an additional O₂ oxidation step after the 5th CH₄/CO₂ redox cycle (Fig. 6). It is clear that a CO₂ peak appeared over BF3 during the O₂ oxidation step, while no carbon oxide (CO and CO₂) peak was verified over the composite CeO₂-BF3, revealing no residual carbon deposition on the CO₂ regenerated CeO₂-BF3 OC. The high resistance towards carbon deposition should be an important factor for the retention of high cyclic stability of CeO₂-BF3.

3.3. Microstructure evolution during the CH₄/CO₂ redox cycles

To uncover the underlying mechanism for outstanding carbon resistance of recycled CeO₂-BF3 OC, the detailed structure evolution under the periodic CH₄/CO₂ redox cycles was carefully investigated with CeO₂, Ce-Fe-Al and BF3 for comparison.

3.3.1. XRD and Rietveld refinement

Fig. 7 shows the XRD patterns of CeO₂, Ce-Fe-Al, BF3 and CeO₂-BF3 OCs during the successive CH₄/CO₂ operation. CeO₂ OC (Fig. 7a) only exhibited cubic fluorite CeO₂ phase after 20 CH₄/CO₂ redox cycles. For BF3 OC (Fig. 7b), the initial charge-insufficient Ba²⁺-MP type hexaaluminate phase transformed to charge-excess Ba²⁺-β-Al₂O₃ phase during the 2nd CH₄ reduction process due to the reduction of Fe³⁺→Fe²⁺ ions via the charge compensation mechanism [36,46]. Meanwhile, weak

signals assigned to FeAl₂O₄ and Fe⁰ were detected due to extraction of lattice oxygen by CH₄ reduction. After the 2nd-20th CH₄/CO₂ redox cycles, the diffraction peaks of both BaAl₂O₄ and FeAl₂O₄ intensified, indicating that part of Fe species in hexaaluminate were gradually stabilized in FeAl₂O₄ spinel with low oxygen storage capacity [48]. The appearance of metallic Fe⁰ and the increased FeAl₂O₄ phase should be responsible for the carbon deposition of BF3 hexaaluminate during the 2nd-20th reduction process (Fig. 5b). However, the β-Al₂O₃ hexaaluminate still presented as the main phase, which may account for the high stability of BF3 for CH₄ conversion (Fig. 5a), since hexaaluminates are attractive catalysts in the high-temperature reactions involving methane conversion [33–35].

Fresh Ce-Fe-Al OC (Fig. 7c) showed multiple phases including CeO₂, α-Fe₂O₃ and α-Al₂O₃. After the 2nd reduction, besides the appearance of trace of FeAl₂O₄ and metallic Fe⁰, characteristic peaks of CeAlO₃ [JCPDS 00-028-0260] with perovskite structure were also observed, indicating the formation of CeAlO₃. During subsequent CH₄/CO₂ redox cycles, both CeAlO₃ and FeAl₂O₄ gradually became the main phases, indicating that Fe species were mainly stabilized in FeAl₂O₄ spinel. For CeO₂-BF3 OC (Fig. 7d), phase transition of MP → β-Al₂O₃ and CeO₂ → CeAlO₃, and formation of metallic Fe⁰ also took place during the 2nd reduction process. After CO₂ oxidation, the diffraction peaks of CeAlO₃ gradually intensified with weakened signals of CeO₂. Although CeAlO₃ phase was formed in both recycled Ce-Fe-Al and CeO₂-BF3 OCs, the diffraction peaks of CeAlO₃ in the 20th recycled CeO₂-BF3 OC significantly shifted to lower 2θ values (Fig. 7e). This demonstrates that larger Fe ions (0.64 Å) might be incorporated into the CeAlO₃ structure to form CeFe_xAl_{1-x}O₃ by replacing smaller Al³⁺ (0.51 Å).

In order to identify the existence of Fe ions in CeFe_xAl_{1-x}O₃ over the recycled CeO₂-BF3 OC, we performed Rietveld XRD refinement analysis, which is a powerful tool to identify the crystalline structure [43,49]. Fig. 8 displays the XRD pattern fitted using the Rietveld refinement method for the CeO₂-BF3 after 20 CH₄/CO₂ redox cycles, and the obtained data is reported in Table 1. The recycled CeO₂-BF3 sample consists of 43.39% β-Al₂O₃, 21.78% CeFe_xAl_{1-x}O₃, 22.98% FeAl₂O₄, 9.86% BaAl₂O₄, and 1.99% CeO₂. Among them, FeAl₂O₄ possesses low oxygen-storage capacity, which may lead to carbon deposition. BaAl₂O₄ is not responsible for changes in the oxidation state and, thus, could not participate in the redox reaction. However, the expected carbon deposition and low reactivity were not observed. The excellent reactivity and high carbon resistance of recycled CeO₂-BF3 were mainly attributed to β-Al₂O₃ hexaaluminate and CeFe_xAl_{1-x}O₃. The phase compositions of β-Al₂O₃ and CeFe_xAl_{1-x}O₃ are Ba_{0.75}Fe_{0.83}Al_{10.17}O_{17.25} and CeFe_{0.24}Al_{0.76}O₃, respectively. The lattice constant *a* (*a*=*b*=*c*) of CeFe_xAl_{1-x}O₃ was 3.779 Å, which was larger than that of standard CeAlO₃ (3.767 Å). Namely, larger Fe ions indeed entered into the CeAlO₃ structure, and about 24% Al sites in CeAlO₃ were occupied by Fe

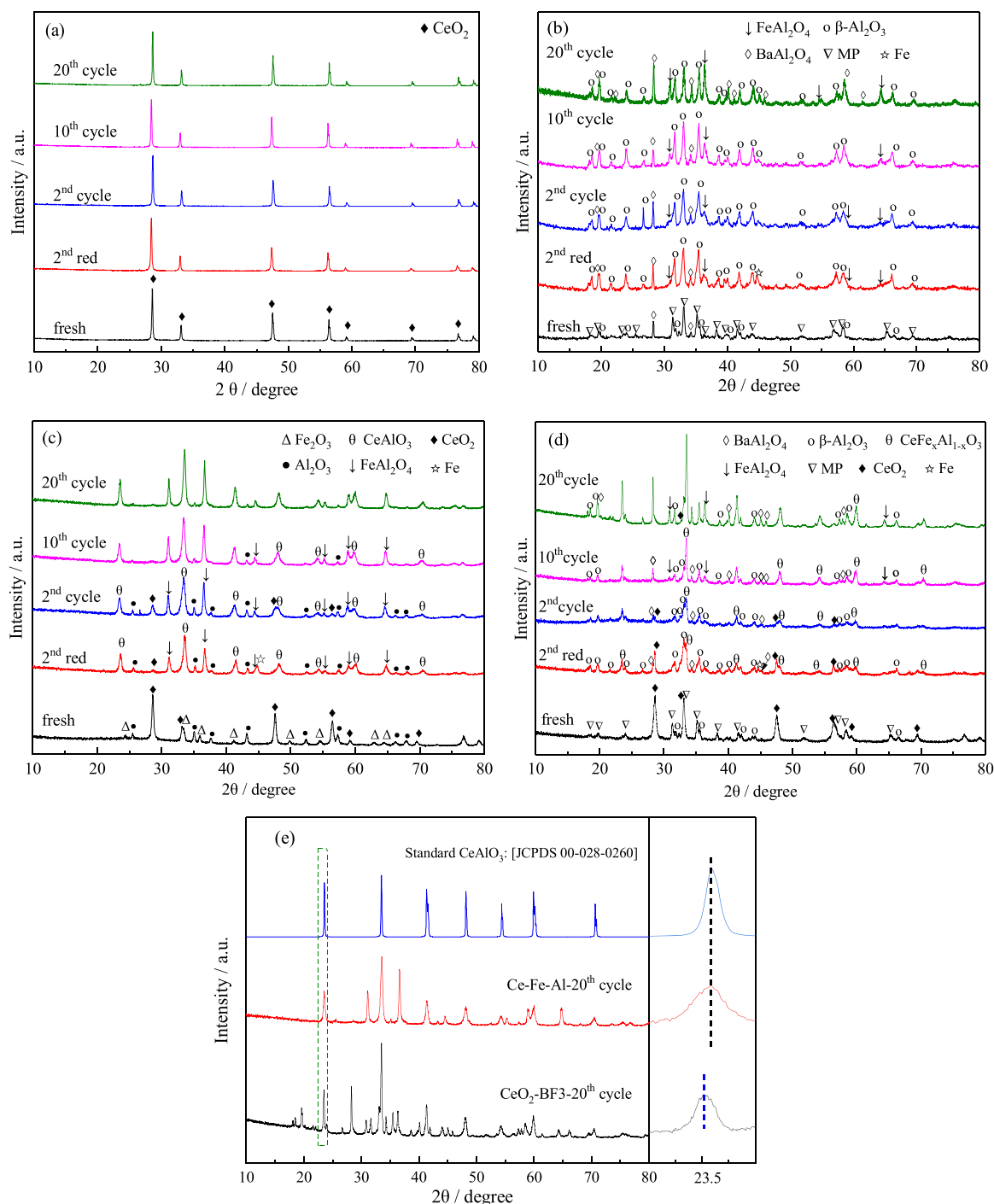


Fig. 7. X-ray diffraction patterns of (a) CeO_2 , (b) BF_3 , (c) Ce-Fe-Al , (d) $\text{CeO}_2\text{-BF}_3$ OCs at various CLDR reaction cycles and (e) both Ce-Fe-Al and $\text{CeO}_2\text{-BF}_3$ OCs after 20 CH_4/CO_2 redox cycles with standard CeAlO_3 for comparison.

ions. The formation of $\text{CeFe}_x\text{Al}_{1-x}\text{O}_3$ ($x = 0.24$) over the recycled $\text{CeO}_2\text{-BF}_3$ OC was probably originated from the strong interaction between CeO_2 and the adjacent Fe and Al ions in the $\text{BaFe}_3\text{Al}_9\text{O}_{19}$ hexaaluminate structure.

To gain an insight into the evolution of $\text{CeFe}_x\text{Al}_{1-x}\text{O}_3$ under redox atmosphere, XRD patterns of $\text{CeO}_2\text{-BF}_3$ after CH_4 reduction, CO_2 and O_2 oxidation were compared. As shown in Fig. 9, CeAlO_3 phase [JCPDS 00-028-0260] appeared after methane reduction only for 4 min. With further reduction, the diffraction peaks of CeAlO_3 slightly shifted to lower 2θ values, which may be caused by the incorporation of Fe ions or the increase of oxygen vacancies. In addition, the characteristic peak

assigned to metallic Fe^0 [JCPDS 98-063-1724] at 44.7° was detected. Since the original Fe ions are stabilized in the hexaaluminate structure that possessing high CH_4 reactivity, the appeared metallic Fe^0 should originate from the reduction of Fe-hexaaluminate by CH_4 . After CO_2 oxidation, the Fe^0 phase disappeared while the diffraction peaks of CeAlO_3 further shifted to lower 2θ values. This confirmed that Fe ions with larger radius, which bleed-out from hexaaluminate, entered into CeAlO_3 to form $\text{CeFe}_x\text{Al}_{1-x}\text{O}_3$ during the CO_2 oxidation period, indicating the stability of $\text{CeFe}_x\text{Al}_{1-x}\text{O}_3$ phase under CO_2 oxidative atmosphere. However, using O_2 as oxidant, the $\text{CeFe}_x\text{Al}_{1-x}\text{O}_3$ phase gradually weakened and completely transformed into CeO_2 phase (Fig. 9).

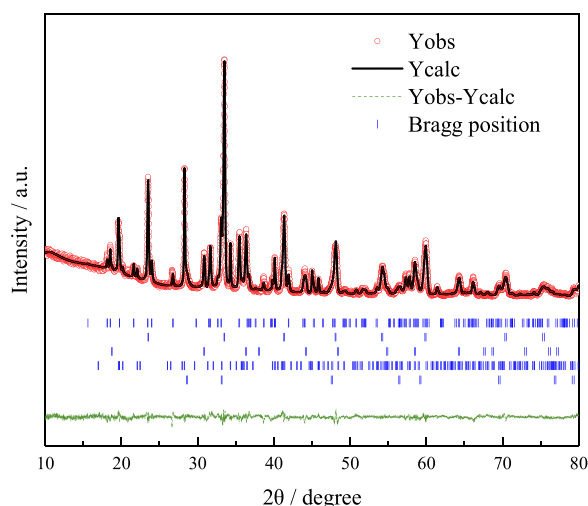


Fig. 8. X-ray diffraction pattern fitted using the Rietveld refinement method for CeO₂-BF3 OC after 20 CH₄/CO₂ redox cycles.

Table 1

Results of Rietveld refinement on the CeO₂-BF3 after 20 CH₄/CO₂ redox cycles.

Result	CeO ₂ -BF3 after 20 cycles
Rp	5.26
Rwp	5.45
Phase proportion (mass ratio)	43.39%β-Al ₂ O ₃ ^a , 21.78%CeFe _x Al _{1-x} O ₃ ^b , 22.98% FeAl ₂ O ₄ ^c , 9.86%BaAl ₂ O ₄ ^d , 1.99%CeO ₂ ^e
Phase composition of β-Al ₂ O ₃	Ba _{0.75} Fe _{0.83} Al _{10.17} O _{17.25}
a=b (Å)	5.647
c ₀ (Å)	22.731
Phase composition of CeFe _x Al _{1-x} O ₃	CeFe _{0.24} Al _{0.76} O ₃
a=b=c (Å)	3.779

^a The atomic coordinates of β-Al₂O₃ phase were taken from reference (JCPDS 01-075-0707, Ba_{0.75}Al₁₁O_{17.25}, Hexagonal system, P63/mmc space group).

^b The atomic coordinates of CeFe_xAl_{1-x}O₃ phase were taken from reference (JCPDS 00-028-0260, CeAlO₃, Cubic system, Pm-3 m space group).

^c The atomic coordinates of FeAl₂O₄ phase were taken from reference (JCPDS 96-900-1982, FeAl₂O₄, Cubic system, Fd-3 m space group).

^d The atomic coordinates of BaAl₂O₄ phase were taken from reference (JCPDS 96-100-8090, BaAl₂O₄, Hexagonal system, P6322 space group).

^e The atomic coordinates of CeO₂ phase were taken from reference (JCPDS 96-900-9009, CeO₂, Cubic system, Fm-3 m space group).

Considering the great discrepancy of phase composition and reaction behaviors between CO₂ and O₂ regenerated/fresh CeO₂-BF3 OCs (Figs. 9 and S4), the formation of CeFe_xAl_{1-x}O₃ phase after the CH₄/CO₂ reaction should be vital for the improved methane-to-syngas conversion.

3.3.2. HRTEM and STEM-EDS

The CeO₂-BF3 OC after 20 CH₄/CO₂ redox cycles was also investigated at the nanometer scale by HRTEM and HAADF-STEM combined with EDS mapping (Fig. 10). The small aggregates (red circle in Fig. 10a) presented the uniform distribution of Ba, Fe, Al and O elements in close vicinity to each other. Corresponding HRTEM image (Fig. 10b) exhibited well-resolved lattice fringes with 2.70 Å assigned to (107) plane of hexaaluminate, indicating the retention of BaFe_xAl_{12-x}O₁₉ hexaaluminate. Close to hexaaluminates, a Ce-rich particle (highlighted by orange oval) was observed, which should be related to the formed CeFe_xAl_{1-x}O₃ particle. Corresponding EDS line-scan profile (Fig. 10c) verified the presence of Fe in CeFe_xAl_{1-x}O₃, in good agreement with the XRD Rietveld refinement analysis.

In order to understand the spatial distribution of CeFe_xAl_{1-x}O₃ during the CH₄ reduction process, HAADF-STEM combined with EDS mapping and line-scan was carried out over reduced CeO₂-BF3 OC. As shown in Fig. 11, besides the nonuniform distribution of Ce, separate Fe islands with low O concentration were also found. The Fe islands are close to hexaaluminates (red circle in Fig. 11a and c), since they originate from the exsolution of Fe species of hexaaluminates due to the continuous extraction of lattice oxygen as discussed in XRD section. The Fe islands are also in intimate contact with CeFe_xAl_{1-x}O₃ (orange oval in Fig. 11a and c). Fig. 11b showed the typical line-scan profile, where the reduced Fe⁰ islands are always sandwiched between hexaaluminate and CeFe_xAl_{1-x}O₃. Such a unique hexaaluminate/Fe⁰/CeFe_xAl_{1-x}O₃ sandwich-like structure was further visualized from the HRTEM images in Fig. 11d. In other words, the formed CeFe_xAl_{1-x}O₃ was in close contact with the reduced Fe⁰ exsolved from Fe-hexaaluminate, which could provide a convenient pathway for the supply of oxygen from CeFe_xAl_{1-x}O₃ to the adjacent reduced Fe⁰ to remove the carbon species in time.

3.4. The effect of in-situ formed CeFe_xAl_{1-x}O₃ phase on oxygen mobility

3.4.1. CH₄-IR

As for methane anaerobic oxidation, CO formation strongly depended on the mobility of lattice oxygen [27,50], which could be used as a reference for oxygen mobility analysis. CH₄-IR (Fig. 12) was conducted to study the CO evolution with temperature over CeO₂-BF3. Compared to O₂-regenerated sample, the CO₂-regenerated CeO₂-BF3 OC with the

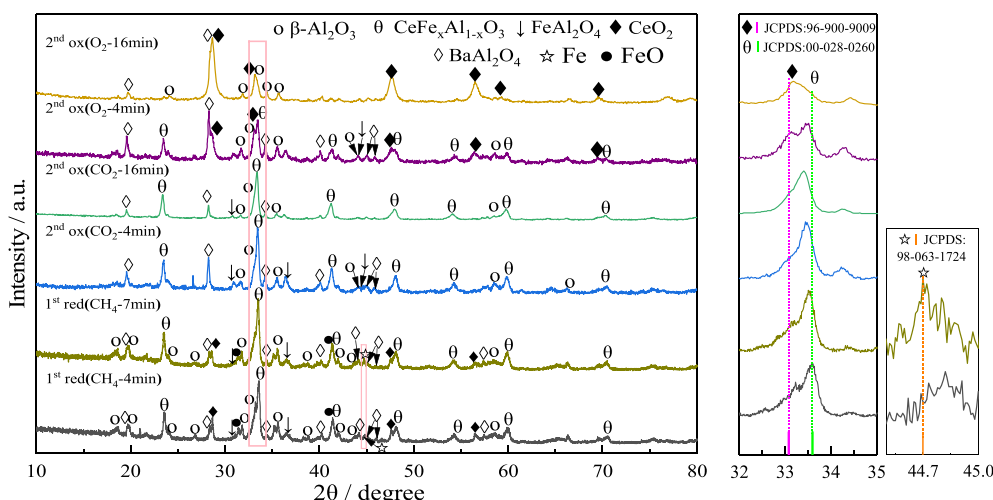


Fig. 9. X-ray diffraction patterns of CeO₂-BF3 after CH₄ reduction, CO₂ and O₂ oxidation with corresponding magnified view.

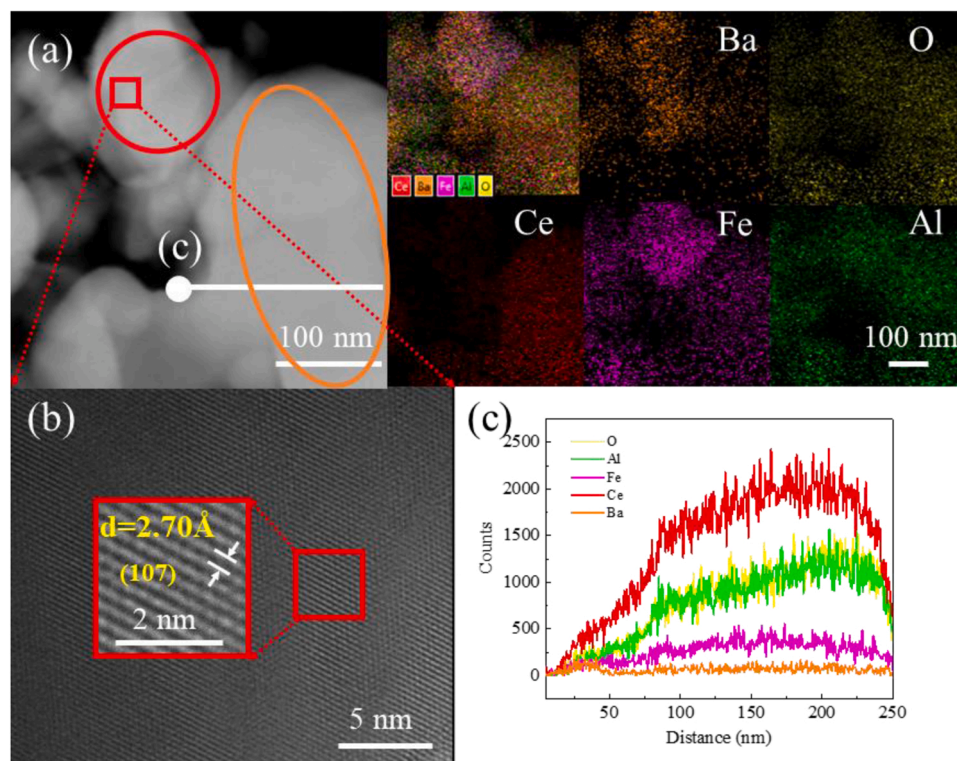


Fig. 10. The images of $\text{CeO}_2\text{-BF3}$ after 20 CH_4/CO_2 redox cycles, (a) HAADF-STEM image with EDS mapping (red circle: hexaaluminate; orange oval: $\text{CeFe}_x\text{Al}_{1-x}\text{O}_3$), and the corresponding (b) HRTEM image, (c) Line-scan profile.

formation of $\text{CeFe}_x\text{Al}_{1-x}\text{O}_3$ phase presented not only lower temperature for CO formation (832°C vs 850°C for O_2 -regenerated OC) but also much higher CO concentration. This strongly suggested the beneficial role of $\text{CeFe}_x\text{Al}_{1-x}\text{O}_3$ phase in enhancing the oxygen mobility.

3.4.2. XPS

The phase transformation from CeO_2 to $\text{CeFe}_x\text{Al}_{1-x}\text{O}_3$ and the successive CH_4/CO_2 redox reaction probably resulted in the surface chemical composition and elementary valence changes. XPS was performed over both BF3 and $\text{CeO}_2\text{-BF3}$ for fresh and recycled samples.

The oxidation states of Ce were analyzed by fitting the curves of Ce 3d XPS spectra in Fig. 13a. The v-u, v'-u' and v''-u'' doublets are assigned to Ce^{4+} state, while the v'-u' peaks verified the presence of Ce^{3+} ions [51]. It is noted that about 14.4% Ce^{3+} ions appeared in the fresh $\text{CeO}_2\text{-BF3}$ sample, which was probably originated from the strong interaction between CeO_2 and BF3 hexaaluminate. After twenty periodic CH_4/CO_2 redox treatment, the relative intensity of v'-u' doublets to the other six bands remarkably enhanced, indicating the significant increase of Ce^{3+} proportion (14.4→31.9%, Table 2), which was ascribed to the formation of $\text{CeFe}_x\text{Al}_{1-x}\text{O}_3$.

In the Fe 2p spectra (Fig. 13b), both fresh BF3 and $\text{CeO}_2\text{-BF3}$ OCs showed the characteristic peaks for Fe $2p_{1/2}$ at ~ 724.4 and 726.9 eV, Fe $2p_{3/2}$ at ~ 711.6 and 715.0 eV, and the satellite at around ~ 718.8 eV that assigned to Fe^{3+} ions [52]. After 20 CH_4/CO_2 redox cycles, the position of Fe 2p spectra shifted to lower B.E. values, and a new peak at ~ 709.9 eV for Fe $2p_{3/2}$ was observed, which verified the presence of Fe^{2+} ions [24]. This was attributed to the weak oxidation ability of CO_2 , which could not completely oxidize Fe^{2+} to the original Fe^{3+} state. To be noted, the recycled $\text{CeO}_2\text{-BF3}$ exhibited higher Fe^{2+} proportion (about 41% vs 30%) than that of BF3, indicating that the intimate interaction between $\text{CeFe}_x\text{Al}_{1-x}\text{O}_3$ and hexaaluminate favors the formation of Fe^{2+} , which may induce more oxygen vacancies.

The distribution of oxygen species was also analyzed. In O 1s XPS spectra (Fig. 13c), the oxygen species can be divided into three

categories in a descending order of the binding energy. The peak (labeled as O I) with a higher binding energy (~ 532.3 eV) is characteristic of the surface oxygen, the peak at ~ 531.3 eV is ascribed to the oxygen defects (e.g., oxygen vacancies, labeled as O II), and the peak at ~ 530.1 eV is attributed to lattice oxygen species (labeled as O III) [53]. The creation of oxygen vacancies is closely related to the lattice oxygen mobility [24,54–56]. From Table 2, one can see that both the introduction of CeO_2 into BF3 and CH_4/CO_2 redox treatment significantly increased the proportion of oxygen defects (O II). In comparison to BF3 (O II, 21.7–32.6%) and fresh $\text{CeO}_2\text{-BF3}$ (O II, 28.6%), the recycled $\text{CeO}_2\text{-BF3}$ OC presented the highest concentration of oxygen defects (O II, 42.4%).

3.4.3. DFT calculation

The oxygen mobility of $\text{CeFe}_x\text{Al}_{1-x}\text{O}_3$ was further quantitatively estimated by DFT calculation. For the convenience of calculation, the model of $\text{CeFe}_{0.25}\text{Al}_{0.75}\text{O}_3$ (cubic structure, Pm-3 m space group) with close composition to $\text{CeFe}_{0.24}\text{Al}_{0.76}\text{O}_3$ (Rietveld refinement result in Table 1) was built with pure CeAlO_3 for comparison. It was found that the lattice constant of $\text{CeFe}_{0.25}\text{Al}_{0.75}\text{O}_3$ was higher than that of CeAlO_3 (3.846 vs 3.797 Å, Table 3) after optimizing the systems, which was ascribed to the fact that Fe^{3+} with larger ionic radius replaced smaller Al^{3+} ions. The doping of Fe^{3+} with larger ionic radius also significantly influenced the length of both Fe-O and Ce-O bonds in $\text{CeFe}_{0.25}\text{Al}_{0.75}\text{O}_3$. The Fe-O bond in $\text{CeFe}_{0.25}\text{Al}_{0.75}\text{O}_3$ was calculated to be 1.990 Å, which was longer than Al-O bond (1.899 Å) in CeAlO_3 . In addition, the length of Ce-O bond in $\text{CeFe}_{0.25}\text{Al}_{0.75}\text{O}_3$ (2.720 Å) was greater than that in CeAlO_3 (2.685 Å) due to the lattice expansion. The increase of bond length may weaken the interaction between metal ions and lattice oxygen, resulting in the facile removal of oxygen atoms from the lattice. Thus, the oxygen vacancy formation energy ($E_{f,vac}$) at three different sites (Fig. S5) were further calculated. For pure cubic CeAlO_3 , the $E_{f,vac}$ was as high as 6.15 eV. However, once 25% Al^{3+} was substituted by Fe^{3+} , the $E_{f,vac}$ at O_1 , O_2 and O_3 sharply reduced to 4.09, 5.68 and

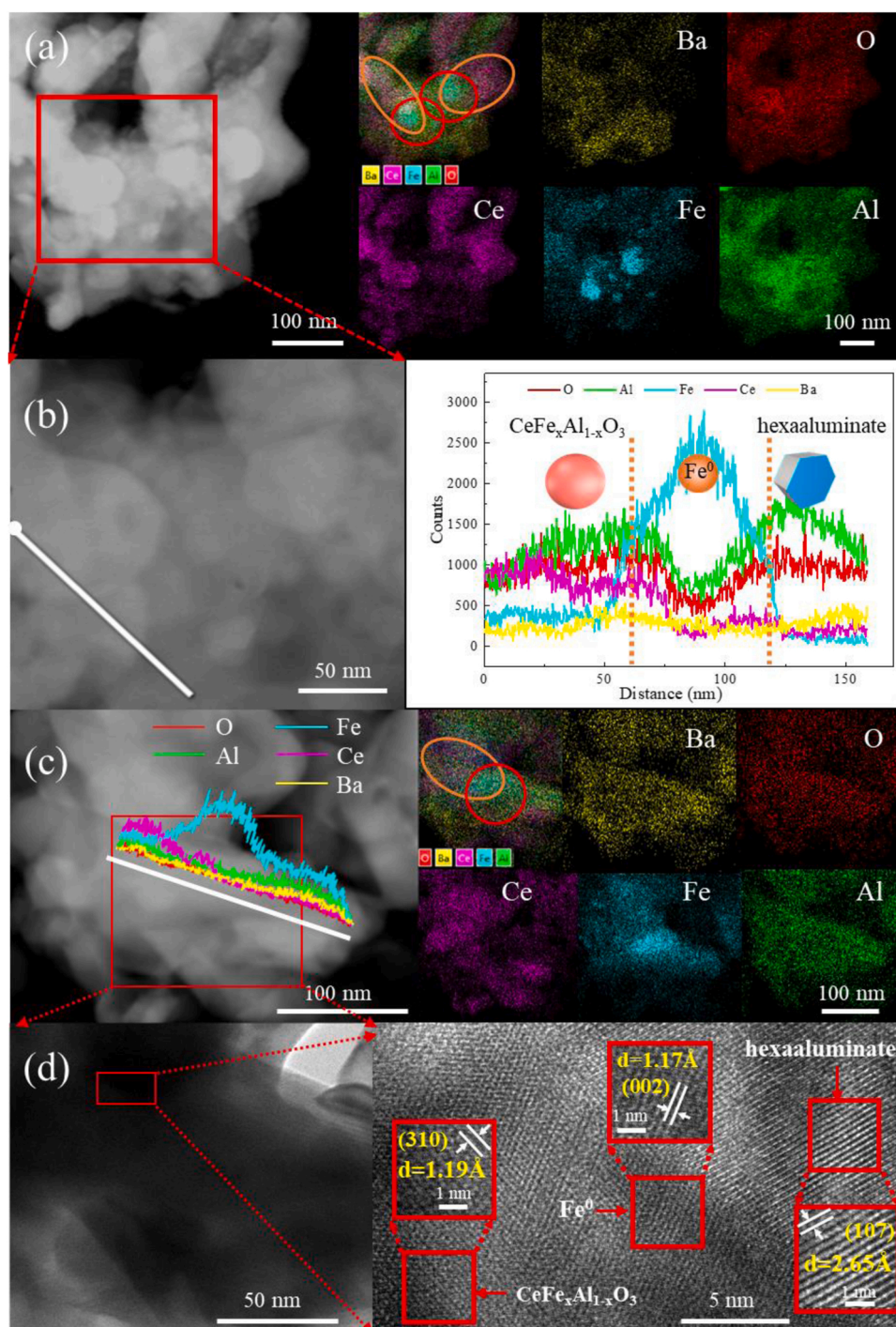


Fig. 11. The images of $\text{CeO}_2\text{-BF}_3$ after the CH_4 reduction for 4 min, (a) HAADF-STEM images with EDS mapping (red circle: hexaaluminate; orange oval: $\text{CeFe}_x\text{Al}_{1-x}\text{O}_3$), (b) STEM image with the corresponding line-scan profile, (c) HAADF-STEM image with EDS mapping and line-scan profile, (d) HRTEM image and the enlarged-view of selected area.

4.52 eV, respectively, which is favorable for the formation of oxygen vacancy [57].

4. Discussion

4.1. The formation of metallic Fe^0 for CH_4 activation

The formation of metallic Fe^0 over the Fe-based OC is a key factor that governing the CH_4 activation [21]. In this work, compared to large Fe_2O_3 particles over Ce-Fe-Al oxide, incorporation of Fe ions in BF3

hexaaluminate matrix enables a high dispersion of Fe species over both BF3 and $\text{CeO}_2\text{-BF}_3$ (XRD, Fig. 1), which benefits the reduction of Fe ions (H_2 -TPR, Fig. 2). Hexaaluminates possess peculiar structure consisting of alternate stacking spinel blocks and mirror plane. In comparison to the closely packed spinel block, the loosely packed mirror plane of hexaaluminate is not only the preferential exposure surface [58,59] but also the preferential diffusion route of oxygen [60]. Therefore, oxygen ions in/near the mirror plane of hexaaluminate preferentially reacted with CH_4 [37], rendering facile reduction of Fe cations to metallic Fe^0 . In turn, these emerging metallic Fe^0 species exsolved from

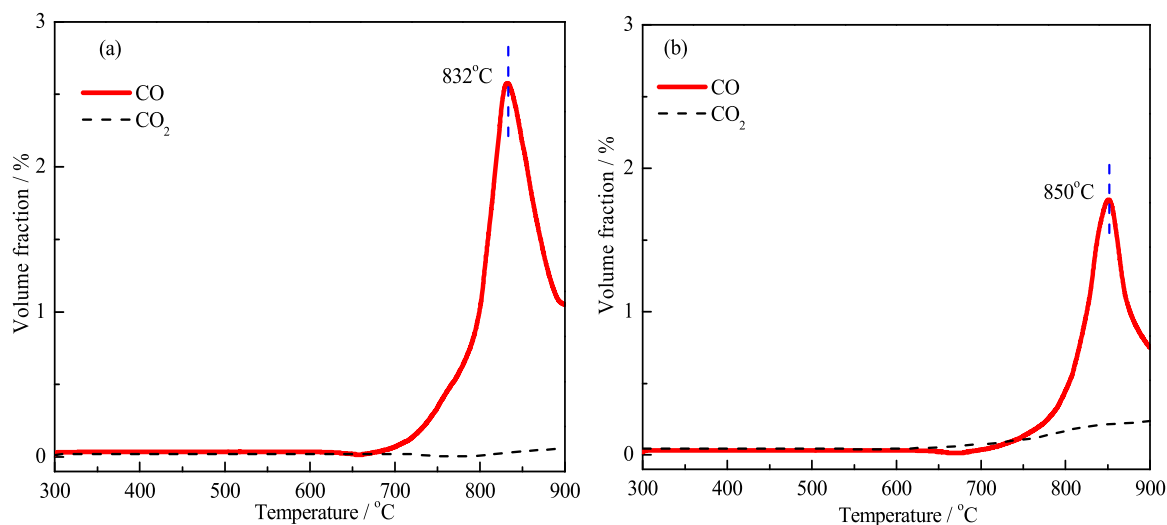


Fig. 12. CH₄-IR profiles of (a) CO₂-generated and (b) O₂-generated CeO₂-BF₃ OCs.

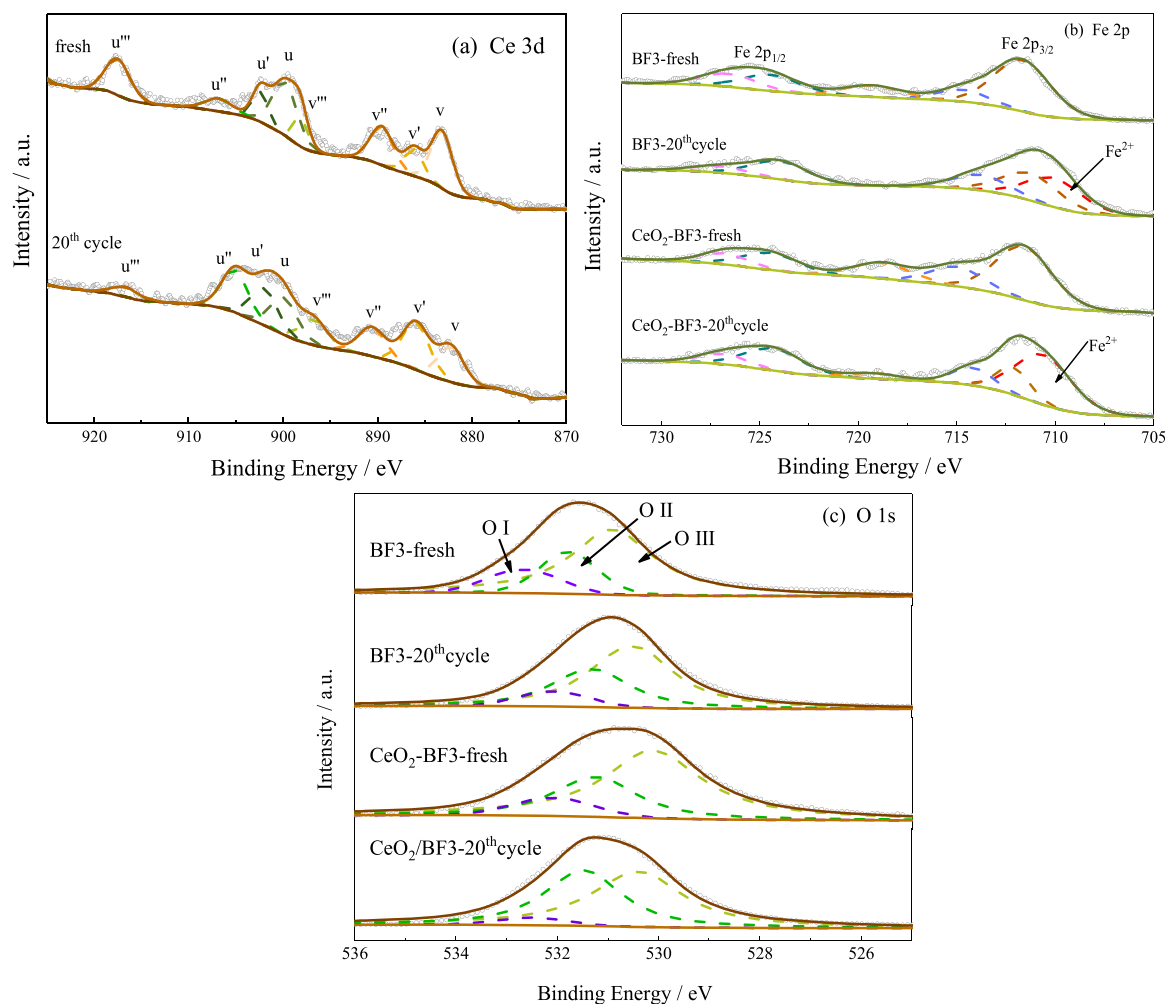


Fig. 13. Ce 3d, Fe 2p and O 1s spectra of BF₃ and CeO₂-BF₃ OCs for fresh and after 20 CH₄/CO₂ redox cycles.

Fe-hexaaluminate could act as more active sites for methane activation. As a result, hexaaluminate-containing BF₃ and CeO₂-BF₃ OCs showed much higher CH₄ conversion (~90%) than both CeO₂ and Ce-Fe-Al (56–68%, Fig. 5a) even after 20 CH₄/CO₂ redox cycles.

4.2. The in-situ formed CeFe_xAl_{1-x}O₃ as oxygen pool

Although metallic Fe⁰ greatly stimulates the methane conversion, it results in high potential to carbon deposition. The carbon removal greatly depended on the “oxygen pool” to supply sufficient lattice

Table 2

Relative percentages of different O, Fe and Ce species in CeO₂-BF3 OCs for fresh and after 20 CH₄/CO₂ redox cycles.

Samples	Ce species percentages (%)		Fe species percentages (%)		O species percentages (%)		
	Ce ⁴⁺	Ce ³⁺	Fe ³⁺	Fe ²⁺	OI	OII	OIII
BF3-fresh	-	-	100	-	14.1	21.7	64.2
BF3-20th cycle	-	-	70.3	29.7	9.0	32.6	58.4
CeO ₂ -BF3-fresh	85.6	14.4	100	-	9.5	28.6	61.9
CeO ₂ -BF3-20th cycle	68.1	31.9	59.0	41.0	4.4	42.4	53.2

Table 3

Lattice parameters and bond lengths of CeAlO₃ and CeFe_{0.25}Al_{0.75}O₃ from DFT calculation.

Structures	Lattice parameter/ Å	Ce-O/ Å	Fe-O/ Å
CeAlO ₃	3.797	2.685	—
CeFe _{0.25} Al _{0.75} O ₃	3.846	2.720	1.990

oxygen in time to oxidize the carbon. For recycled BF3 OC, as the CH₄ reduction proceeding with the formation of metallic Fe⁰, the mirror plane becomes more and more oxygen-depleted, but both the spinel block of hexaaluminate and the newly formed FeAl₂O₄ phase possess the low oxygen-donating capacity due to the strong Fe-O interaction in the rigid spinel structure, thus the formed carbon failed to be oxidized by lattice oxygen in time. Therefore, severe carbon deposition occurred over the recycled BF3 hexaaluminate due to the insufficient lattice oxygen supply.

Once CeFe_xAl_{1-x}O₃ was formed over the recycled CeO₂-BF3, the capacity of oxygen supply was greatly improved (Fig. 14). In our work, CeO₂-hexaaluminate interaction induced the in-situ formation of perovskite-type CeFe_xAl_{1-x}O₃ with the incorporation of Fe ions into CeAlO₃. Rietveld refinement identified the composition of CeFe_xAl_{1-x}O₃ (x = 0.24) phase with about 24% Al sites occupied by Fe ions. Our DFT calculation results revealed that the doping of Fe into CeAlO₃ greatly weakened the strength of both Ce-O and Fe-O bonds and decreased the oxygen vacancy formation energy, which led to the abundant oxygen vacancies identified by XPS (Fig. 13). The abundant oxygen vacancies in CeFe_xAl_{1-x}O₃ endow a favorable oxygen migration, which benefits the supply of lattice oxygen. Besides the sufficient oxygen supply, in-time efficient removal of carbon deposited onto Fe⁰ lies in the close proximity between "oxygen pool" and the carbon. Fortunately, the location of CeFe_xAl_{1-x}O₃ was in close contact with the metallic Fe⁰ exsolved from

Fe-hexaaluminate in a unique hexaaluminate/Fe⁰/CeFe_xAl_{1-x}O₃ sandwich-like structure (visualized from Fig. 11), which provided a convenient pathway for CeFe_xAl_{1-x}O₃ as "oxygen pool" to supply sufficient oxygen for the in-time oxidation of carbon over the adjacent active Fe⁰ species. Consequently, the significantly enhanced methane-to-syngas conversion with outstanding carbon resistance was obtained over the recycled CeO₂-BF3 OC even under the condition of metallic Fe⁰ presence. Furthermore, the CeFe_xAl_{1-x}O₃ phase was stable under CO₂ oxidation atmosphere (Fig. 9), which ensured the exertion of stable sufficient oxygen supply for high carbon resistance during the successive CH₄/CO₂ redox cycles.

5. Conclusion

In summary, the carbon resistance could be greatly improved by in-situ formed CeFe_xAl_{1-x}O₃ over ceria-hexaaluminate as "oxygen pool" even under Fe⁰ coexist condition. It was found that the formation of CeFe_xAl_{1-x}O₃ did not occur in CeO₂-Fe₂O₃-Al₂O₃, but it appears in ceria-hexaaluminate, which was probably originated from the strong interaction between CeO₂ and the adjacent Fe and Al ions in BaFe₃Al₉O₁₉ hexaaluminate structure. CeFe_xAl_{1-x}O₃ had a great beneficial role in increasing the oxygen mobility due to weakened Ce-O/Fe-O bond strength and decreased oxygen vacancy formation energy. The location of CeFe_xAl_{1-x}O₃ was in intimate contact with metallic Fe⁰ exsolved from Fe-hexaaluminate in a unique hexaaluminate/Fe⁰/CeFe_xAl_{1-x}O₃ sandwich-like structure, which provided a convenient pathway for CeFe_xAl_{1-x}O₃ as "oxygen pool" to supply sufficient oxygen for the in-time oxidation of carbon over adjacent Fe⁰. As a result, the recycled CeO₂-BF3 OC presents outstanding carbon resistance and high CH₄ conversion (~90%) with improved syngas productivity, which was about 105% and 72% higher than Ce-Fe-Al oxide and Fe-hexaaluminate, respectively, even under the condition of metallic Fe⁰ presence. The CeFe_xAl_{1-x}O₃ phase was stable under the CO₂ oxidation atmosphere, which ensured the exertion of stable sufficient oxygen supply for high carbon resistance during the successive CH₄/CO₂ redox cycles. The findings in present work suggested that designing OCs that facilitates formation of surface Fe⁰ while possesses stable sufficient oxygen supply for in-time carbon oxidation is essential to achieve both high CH₄ activation and carbon resistance. The strategy of constructing "oxygen pool" can provide meaningful guidance for designing more advanced OCs for efficient CLDR process.

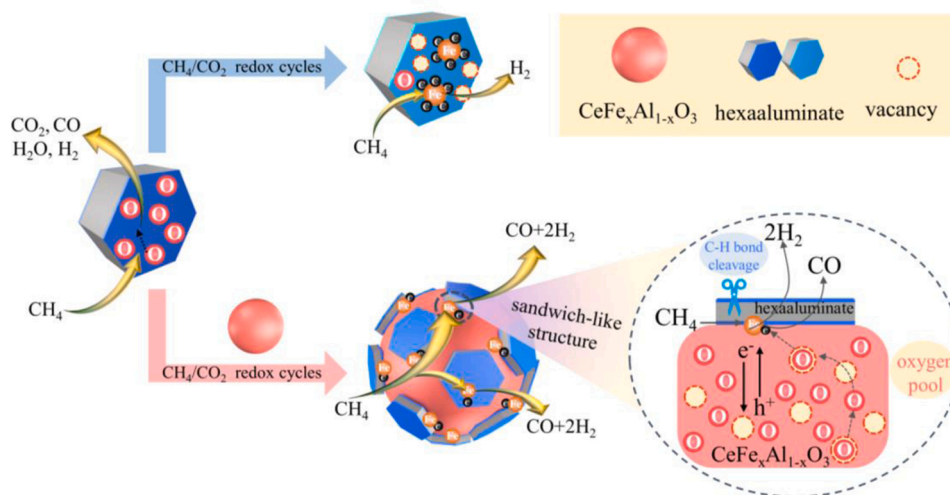


Fig. 14. Schematic diagram of the reaction mechanism over BF3 and CeO₂-BF3 OCs.

CRediT authorship contribution statement

Qian Yang: Methodology, Data curation, Writing – original draft, Validation. **Lihua Chen:** Methodology, Writing – original draft, Software, Visualization. **Nannan Jin:** Data curation, Investigation, Validation. **Yanyan Zhu:** Conceptualization, Validation, Writing – original draft, Funding acquisition, Supervision, Writing – review & editing, Formal analysis, Resources. **Jiahui He:** Software, Visualization, Formal analysis. **Peijie Zhao:** Visualization, Formal analysis. **Chuande Huang:** Validation, Supervision, Writing – review & editing. **Liping Wei:** Formal analysis, Resources. **Xiaoxun Ma:** Project administration, Resources. **Xiaodong Wang:** Project administration, Resources, Writing – review & editing.

Declaration of Competing Interest

The authors declare that they have no known competing financial interests or personal relationships that could have appeared to influence the work reported in this paper.

Data availability

Data will be made available on request.

Acknowledgements

Financial supports from National Science Foundation of China (NSFC) grants (21978239, 21706254 and 22178337, 22278332), Joint Fund of the Yulin University and the Dalian National Laboratory for Clean Energy (2021012), Dalian Institute of Chemical Physics, CAS (DICP I201916) and Cyrus Tang Foundation are gratefully acknowledged.

Appendix A. Supporting information

Supplementary data associated with this article can be found in the online version at [doi:10.1016/j.apcatb.2023.122636](https://doi.org/10.1016/j.apcatb.2023.122636).

References

- [1] A. More, S. Bhavsar, G. Vesper, Iron-nickel alloys for carbon dioxide activation by chemical looping dry reforming of methane, *Energy Technol.* 4 (2016) 1147–1157, <https://doi.org/10.1002/ente.v4.10/>.
- [2] L.C. Buelens, V.V. Galvita, H. Poelman, C. Detavernier, G.B. Marin, Super-dry reforming of methane intensifies CO₂ utilization via Le Chatelier's principle, *Science* 354 (2016) 449–452, <https://doi.org/10.1126/science.aah7161>.
- [3] F. Donat, C.R. Müller, CO₂-free conversion of CH₄ to syngas using chemical looping, *Appl. Catal. B* 278 (2020), 119328, <https://doi.org/10.1016/j.apcatb.2020.119328>.
- [4] V. Shah, Z. Cheng, D.S. Baser, J.A. Fan, L.-S. Fan, Highly selective production of syngas from chemical looping reforming of methane with CO₂ utilization on MgO-supported calcium ferrite redox materials, *Appl. Energy* 282 (2021), 116111, <https://doi.org/10.1016/j.apenergy.2020.116111>.
- [5] D. Pakhare, J. Spivey, A review of dry (CO₂) reforming of methane over noble metal catalysts, *Chem. Soc. Rev.* 43 (2014) 7813–7837, <https://doi.org/10.1039/c3cs60395d>.
- [6] K. Li, X. Chang, C.L. Pei, X.Y. Li, S. Chen, X.H. Zhang, S. Assabumrungrat, Z. J. Zhao, L. Zeng, J.L. Gong, Ordered mesoporous Ni/La₂O₃ catalysts with interfacial synergism towards CO₂ activation in dry reforming of methane, *Appl. Catal. B* 259 (2019), 118092, <https://doi.org/10.1016/j.apcatb.2019.118092>.
- [7] A. Löfberg, J. Guerrero-Caballero, T. Kane, A. Rubbens, L. Jalowiecki-Duhamel, Ni/CeO₂ based catalysts as oxygen vectors for the chemical looping dry reforming of methane for syngas production, *Appl. Catal. B* 212 (2017) 159–174, <https://doi.org/10.1016/j.apcatb.2017.04.048>.
- [8] M. Najera, R. Solunke, T. Gardner, G. Vesper, Carbon capture and utilization via chemical looping dry reforming, *Chem. Eng. Res. Des.* 89 (2011) 1533–1543, <https://doi.org/10.1016/j.cherd.2010.12.017>.
- [9] S. Bhavsar, M. Najera, G. Vesper, Chemical looping dry reforming as novel, intensified process for CO₂ activation, *Chem. Eng. Technol.* 35 (2012) 1281–1290, <https://doi.org/10.1002/ceat.201100649>.
- [10] M.C. Tang, L. Xu, M.H. Fan, Progress in oxygen carrier development of methane-based chemical-looping reforming: a review, *Appl. Energy* 151 (2015) 143–156, <https://doi.org/10.1016/j.apenergy.2015.04.017>.
- [11] A. Shafiearhoo, J.S. Zhang, L.M. Neal, F.X. Li, Rh-promoted mixed oxides for “low-temperature” methane partial oxidation in the absence of gaseous oxidants, *J. Mater. Chem. A* 5 (2017) 11930–11939, <https://doi.org/10.1039/c7ta01398a>.
- [12] L.M. Neal, A. Shafiearhoo, F.X. Li, Dynamic methane partial oxidation using a Fe₂O₃@La_{0.8}Sn_{0.2}FeO_{3-δ} core-shell redox catalyst in the absence of gaseous oxygen, *ACS Catal.* 4 (2014) 3560–3569, <https://doi.org/10.1021/cs5008415>.
- [13] W. Liu, Controlling lattice oxygen activity of oxygen carrier materials by design: a review and perspective, *React. Chem. Eng.* 6 (2021) 1527–1537, <https://doi.org/10.1039/d1re00209k>.
- [14] S. Bhavsar, G. Vesper, Bimetallic Fe–Ni oxygen carriers for chemical looping combustion, *Ind. Eng. Chem. Res.* 52 (2013) 15342–15352, <https://doi.org/10.1021/ie400612g>.
- [15] V.P. Haribal, X.J. Wang, R. Dudek, C. Paulus, B. Turk, R. Gupta, F.X. Li, Modified ceria for “low-temperature” CO₂ utilization: a chemical looping route to exploit industrial waste heat, *Adv. Energy Mater.* 9 (2019) 1901963, <https://doi.org/10.1002/aenm.201901963>.
- [16] D. Hosseini, P.M. Abdala, F. Donat, S.M. Kim, C.R. Müller, Bifunctional core-shell architecture allows stable H₂ production utilizing CH₄ and CO₂ in a catalytic chemical looping process, *Appl. Catal. B* 258 (2019), 117946, <https://doi.org/10.1016/j.apcatb.2019.117946>.
- [17] S.A. Theofanidis, V.V. Galvita, M. Sabbe, H. Poelman, C. Detavernier, G.B. Marin, Controlling the stability of a Fe–Ni reforming catalyst: structural organization of the active components, *Appl. Catal. B* 209 (2017) 405–416, <https://doi.org/10.1016/j.apcatb.2017.03.025>.
- [18] L. Qin, Z. Cheng, M. Guo, M. Xu, J.A. Fan, L.-S. Fan, Impact of 1% lanthanum dopant on carbonaceous fuel redox reactions with an iron-based oxygen carrier in chemical looping processes, *ACS Energy Lett.* 2 (2017) 70–74, <https://doi.org/10.1021/acseenergylett.6b00511>.
- [19] L. Qin, M.Q. Guo, Y. Liu, Z. Cheng, J.A. Fan, L.-S. Fan, Enhanced methane conversion in chemical looping partial oxidation systems using a copper doping modification, *Appl. Catal. B* 235 (2018) 143–149, <https://doi.org/10.1016/j.apcatb.2018.04.072>.
- [20] L. Zhang, Y. Hu, W.B. Xu, C.D. Huang, Y. Su, M. Tian, Y.Y. Zhu, H.M. Gong, X. D. Wang, Anti-coke BaFe_{1-x}Sn_xO_{3-δ} oxygen carriers for enhanced syngas production via chemical looping partial oxidation of methane, *Energy Fuels* 34 (2020) 6991–6998, <https://doi.org/10.1021/acs.energyfuels.0c00951>.
- [21] Y. Kang, Y.J. Han, M. Tian, C.D. Huang, C.J. Wang, J. Lin, B.L. Hou, Y. Su, L. Li, J. H. Wang, X.D. Wang, Promoted methane conversion to syngas over Fe-based garnets via chemical looping, *Appl. Catal. B* 278 (2020), 119305, <https://doi.org/10.1016/j.apcatb.2020.119305>.
- [22] Y.X. Zhang, E. Doroodchi, B. Moghtaderi, Reduction kinetics of Fe₂O₃/Al₂O₃ by ultralow concentration methane under conditions pertinent to chemical looping combustion, *Energy Fuels* 29 (2015) 337–345, <https://doi.org/10.1021/ef5024252>.
- [23] V.V. Galvita, H. Poelman, V. Bliznuk, C. Detavernier, G.B. Marin, CeO₂-modified Fe₂O₃ for CO₂ utilization via chemical looping, *Ind. Eng. Chem. Res.* 52 (2013) 8416–8426, <https://doi.org/10.1021/ie4003574>.
- [24] Y.E. Zheng, K.Z. Li, H. Wang, D. Tian, Y.H. Wang, X. Zhu, Y.G. Wei, M. Zheng, Y. M. Luo, Designed oxygen carriers from macroporous LaFeO₃ supported CeO₂ for chemical-looping reforming of methane, *Appl. Catal. B* 202 (2017) 51–63, <https://doi.org/10.1016/j.apcatb.2016.08.024>.
- [25] X.L. Yin, S. Wang, R. Sun, S.X. Jiang, L.H. Shen, A Ce–Fe oxygen carrier with a core-shell structure for chemical looping steam methane reforming, *Ind. Eng. Chem. Res.* 59 (2020) 9775–9786, <https://doi.org/10.1021/acs.iecr.0c00055>.
- [26] S.W. Ma, M. Li, G.B. Wang, L. Zhang, S.Y. Chen, Z. Sun, J. Hu, M. Zhu, W.G. Xiang, Effects of Zr doping on Fe₂O₃/CeO₂ oxygen carrier in chemical looping hydrogen generation, *Chem. Eng. J.* 346 (2018) 712–725, <https://doi.org/10.1016/j.cej.2018.03.171>.
- [27] K.Z. Li, H. Wang, Y.G. Wei, D.X. Yan, Syngas production from methane and air via a redox process using Ce–Fe mixed oxides as oxygen carriers, *Appl. Catal. B* 97 (2010) 361–372, <https://doi.org/10.1016/j.apcatb.2010.04.018>.
- [28] M.C. Tang, K. Liu, D.M. Roddick, M.H. Fan, Enhanced lattice oxygen reactivity over Fe₂O₃/Al₂O₃ redox catalyst for chemical-looping dry (CO₂) reforming of CH₄: synergistic La–Ce effect, *J. Catal.* 368 (2018) 38–52, <https://doi.org/10.1016/j.jcat.2018.09.022>.
- [29] C.D. Huang, J. Wu, Y.T. Chen, M. Tian, A.I. Rykov, B.L. Hou, J. Lin, C.R. Chang, X. Pan, J.H. Wang, A.Q. Wang, X.D. Wang, In situ encapsulation of iron(0) for solar thermochemical syngas production over iron-based perovskite material, *Commun. Chem.* 1 (2018) 1–55, <https://doi.org/10.1038/s42004-018-0050-y>.
- [30] L. Zhang, W.B. Xu, J. Wu, Y. Hu, C.D. Huang, Y.Y. Zhu, M. Tian, Y. Kang, X.L. Pan, Y. Su, J.H. Wang, X.D. Wang, Identifying the role of A-site cations in modulating oxygen capacity of iron-based perovskite for enhanced chemical looping methane-to-syngas conversion, *ACS Catal.* 10 (2020) 9420–9430, <https://doi.org/10.1021/acscatal.0c01811>.
- [31] O. Mihai, D. Chen, A. Holmen, Chemical looping methane partial oxidation: the effect of the crystal size and O content of LaFeO₃, *J. Catal.* 293 (2012) 175–185, <https://doi.org/10.1016/j.jcat.2012.06.022>.
- [32] N.V.R.A. Dharanipragada, M. Meledina, V.V. Galvita, H. Poelman, S. Turner, G. Van Tendeloo, C. Detavernier, G.B. Marin, Deactivation study of Fe₂O₃–CeO₂ during redox cycles for CO production from CO₂, *Ind. Eng. Chem. Res.* 55 (2016) 5911–5922, <https://doi.org/10.1021/acs.iecr.6b00963>.
- [33] T.H. Gardner, J.J. Spivey, A. Campos, J.C. Hissam, E.L. Kugler, A.D. Roy, Catalytic partial oxidation of CH₄ over Ni-substituted barium hexaaluminate catalysts, *Catal. Today* 157 (2010) 166–169, <https://doi.org/10.1016/j.cattod.2010.05.033>.

- [34] M. Tian, X.D. Wang, T. Zhang, Hexaaluminates: a review of the structure, synthesis and catalytic performance, *Catal. Sci. Technol.* 6 (2016) 1984–2004, <https://doi.org/10.1039/c5cy02077h>.
- [35] F. Huang, X.D. Wang, A.Q. Wang, J.M. Xu, T. Zhang, A two-step synthesis of Fe-substituted hexaaluminates with enhanced surface area and activity in methane catalytic combustion, *Catal. Sci. Technol.* 6 (2016) 4962–4969, <https://doi.org/10.1039/c5cy02187a>.
- [36] Y.Y. Zhu, N.N. Jin, R.L. Liu, X.Y. Sun, L. Bai, H.J. Tian, X.X. Ma, X.D. Wang, Bimetallic $\text{BaFe}_2\text{MAl}_9\text{O}_{19}$ (M = Mn, Ni, and Co) hexaaluminates as oxygen carriers for chemical looping dry reforming of methane, *Appl. Energy* 258 (2020), 114070, <https://doi.org/10.1016/j.apenergy.2019.114070>.
- [37] Y.Y. Zhu, W.W. Liu, X.Y. Sun, X.X. Ma, Y. Kang, X.D. Wang, J.H. Wang, La-hexaaluminate for synthesis gas generation by chemical looping partial oxidation of methane using CO_2 as sole oxidant, *AIChE J.* 64 (2018) 550–563, <https://doi.org/10.1002/aic.15942>.
- [38] S. Bhavsar, G. Vesper, Reducible supports for Ni-based oxygen carriers in chemical looping combustion, *Energy Fuels* 27 (2013) 2073–2084, <https://doi.org/10.1021/ef400184b>.
- [39] Y.Y. Zhu, X.Y. Sun, W.W. Liu, P. Xue, M. Tian, X.D. Wang, X.X. Ma, T. Zhang, Microstructure and reactivity evolution of La-Fe-Al oxygen carrier for syngas production via chemical looping $\text{CH}_4\text{-CO}_2$ reforming, *Int. J. Hydrog. Energy* 42 (2017) 30509–30524, <https://doi.org/10.1016/j.ijhydene.2017.10.037>.
- [40] B. Delley, From molecules to solids with the DMol³ approach, *J. Chem. Phys.* 113 (2000) 7756–7764, <https://doi.org/10.1063/1.1316015>.
- [41] J.P. Perdew, K. Burke, M. Ernzerhof, Generalized gradient approximation made simple, *Phys. Rev. Lett.* 77 (1996) 3865–3868, <https://doi.org/10.1103/PhysRevLett.77.1396>.
- [42] Y.Y. Zhu, X.D. Wang, G.T. Wu, Y.Q. Huang, Y. Zhang, J.H. Wang, T. Zhang, Evolution of Fe crystallographic sites from barium hexaaluminate to hexaferrite, *J. Phys. Chem. C* 116 (2011) 671–680, <https://doi.org/10.1021/jp2067414>.
- [43] Y.Y. Zhu, X.D. Wang, A.Q. Wang, G.T. Wu, J.H. Wang, T. Zhang, Identification of the chemical state of Fe in barium hexaaluminate using Rietveld refinement and ⁵⁷Fe Mössbauer spectroscopy, *J. Catal.* 283 (2011) 149–160, <https://doi.org/10.1016/j.jcat.2011.08.001>.
- [44] X. Zhu, Y.G. Wei, H. Wang, K.Z. Li, Ce-Fe oxygen carriers for chemical-looping steam methane reforming, *Int. J. Hydrog. Energy* 38 (2013) 4492–4501, <https://doi.org/10.1016/j.ijhydene.2013.01.115>.
- [45] Z. Cheng, L. Zhang, N.N. Jin, Y.Y. Zhu, L.H. Chen, Q. Yang, M. Yan, X.X. Ma, X. D. Wang, Effect of calcination temperature on the performance of hexaaluminate supported CeO_2 for chemical looping dry reforming, *Fuel Process. Technol.* 218 (2021), 106873, <https://doi.org/10.1016/j.fuproc.2021.106873>.
- [46] Y.Y. Zhu, R.L. Liu, X.Y. Sun, X.X. Ma, X.D. Wang, H.J. Tian, Metal modified hexaaluminates for syngas generation and CO_2 utilization via chemical looping, *Int. J. Hydrog. Energy* 44 (2019) 10218–10231, <https://doi.org/10.1016/j.ijhydene.2019.02.187>.
- [47] S. Bhavsar, G. Vesper, Chemical looping beyond combustion: production of synthesis gas via chemical looping partial oxidation of methane, *RSC Adv.* 4 (2014) 47254–47267, <https://doi.org/10.1039/c4ra06437b>.
- [48] L.K. Rihko-Struckmann, P. Datta, M. Wenzel, K. Sundmacher, N.V.R. A. Dharanipragada, H. Poelman, V.V. Galvita, G.B. Marin, Hydrogen and carbon monoxide production by chemical looping over iron-aluminium oxides, *Energy Technol.* 4 (2016) 304–313, <https://doi.org/10.1002/ente.201500231>.
- [49] Y.Y. Zhu, X.D. Wang, Y.Q. Huang, Y. Zhang, G.T. Wu, J.H. Wang, T. Zhang, Identification of the crystallographic sites of Ir in $\text{BaIr}_{0.2}\text{FeAl}_{0.8}\text{O}_{19}$ hexaaluminate, *J. Phys. Chem. C* 116 (2012) 24487–24495, <https://doi.org/10.1021/jp3007238>.
- [50] X.H. Zhang, C.L. Pei, X. Chang, S. Chen, R. Liu, Z.J. Zhao, R. Mu, J.L. Gong, FeO_6 octahedral distortion activates lattice oxygen in perovskite ferrite for methane partial oxidation coupled with CO_2 splitting, *J. Am. Chem. Soc.* 142 (2020) 11540–11549, <https://doi.org/10.1021/jacs.0c04643>.
- [51] R. Si, Y.W. Zhang, S.J. Li, B.X. Lin, C.H. Yan, Urea-based hydrothermally derived homogeneous nanostructured $\text{Ce}_{1-x}\text{Zr}_x\text{O}_2$ ($x=0\text{--}0.8$) solid solutions: correlation between oxygen storage capacity and lattice strain, *J. Phys. Chem. C* 108 (2004) 12481–12488, <https://doi.org/10.1021/jp048084b>.
- [52] S. Thirumalaiah, K. Girija, N.Y. Hebalkar, D. Mangalaraj, C. Viswanathan, N. Ponpandian, Shape evolution of perovskite LaFeO_3 nanostructures: a systematic investigation of growth mechanism, properties and morphology dependent photocatalytic activities, *RSC Adv.* 3 (2013) 7549–7561, <https://doi.org/10.1039/c3ra00006k>.
- [53] X. Zhu, K.Z. Li, Y.G. Wei, H. Wang, L.Y. Sun, Chemical-looping steam methane reforming over a $\text{CeO}_2\text{-Fe}_2\text{O}_3$ oxygen carrier: evolution of its structure and reducibility, *Energy Fuels* 28 (2014) 754–760, <https://doi.org/10.1021/ef402203a>.
- [54] H. Chang, E. Bjørgum, O. Mihai, J. Yang, H.L. Lein, T. Grande, S. Raaen, Y.A. Zhu, A. Holmen, D. Chen, Effects of oxygen mobility in La-Fe-based perovskites on the catalytic activity and selectivity of methane oxidation, *ACS Catal.* 10 (2020) 3707–3719, <https://doi.org/10.1021/acscatal.9b05154>.
- [55] Z. Ma, S. Zhang, R. Xiao, J.F. Wang, Inhibited phase segregation to enhance the redox performance of NiFe_2O_4 via CeO_2 modification in the chemical looping process, *Energy Fuels* 34 (2020) 6178–6185, <https://doi.org/10.1021/acs.energyfuels.0c00686>.
- [56] F. Liu, L.Y. Chen, J.K. Neathery, K. Saito, K.L. Liu, Cerium oxide promoted iron-based oxygen carrier for chemical looping combustion, *Ind. Eng. Chem. Res.* 53 (2014) 16341–16348, <https://doi.org/10.1021/ie503160b>.
- [57] A.B. Munoz-Garcia, D.E. Bugaris, M. Pavone, J.P. Hodges, A. Huq, F.L. Chen, Z.H. C. Loye, E.A. Carter, Unveiling structure-property relationships in $\text{Sr}_2\text{Fe}_{1.5}\text{Mo}_{0.5}\text{O}_{6-\delta}$, an electrode material for symmetric solid oxide fuel cells, *J. Am. Chem. Soc.* 134 (2012) 6826–6833, <https://doi.org/10.1021/ja300831k>.
- [58] G. Groppi, F. Assandri, M. Bellotto, C. Cristiani, P. Forzatti, The crystal structure of Ba- β -alumina materials for high-temperature catalytic combustion, *J. Solid State Chem.* 114 (1995) 326–336, <https://doi.org/10.1006/jcat.1998.2220>.
- [59] M. Bellotto, G. Artioli, C. Cristiani, P. Forzatti, G. Groppi, On the crystal structure and cation valence of Mn in Mn-substituted Ba- β - Al_2O_3 , *J. Catal.* 179 (1998) 597–605, <https://doi.org/10.1006/jcat.1998.2220>.
- [60] M. Machida, A. Sato, T. Kijima, H. Inoue, K. Eguchi, H. Arai, Catalytic properties and surface modification of hexaaluminate microcrystals for combustion catalyst, *Catal. Today* 26 (1995) 239–245, [https://doi.org/10.1016/0920-5861\(95\)00145-3](https://doi.org/10.1016/0920-5861(95)00145-3).